ELEMENTA Science of the Anthropocene

Harasyn, ML, et al. 2020. Multi-scale observations of the co-evolution of sea ice thermophysical properties and microwave brightness temperatures during the summer melt period in Hudson Bay. *Elem Sci Anth,* 8: 16. DOI: https://doi.org/10.1525/elementa.412

RESEARCH ARTICLE

Multi-scale observations of the co-evolution of sea ice thermophysical properties and microwave brightness temperatures during the summer melt period in Hudson Bay

Madison L. Harasyn*, Dustin Isleifson*,†, Wayne Chan* and David G. Barber*

Monitoring the trend of sea ice breakup and formation in Hudson Bay is vital for maritime operations, such as local hunting or shipping, particularly in response to the lengthening of the ice-free period in the Bay driven by climate change. Satellite passive microwave sea ice concentration products are commonly used for large-scale sea ice monitoring and predictive modelling; however, these product algorithms are known to underperform during the summer melt period due to the changes in sea ice thermophysical properties. This study investigates the evolution of *in situ* and satellite-retrieved brightness temperature (T_B) throughout the melt season using a combination of *in situ* passive microwave measurements, thermophysical sampling, unmanned aerial vehicle (UAV) surveys, and satellite-retrieved T_B. *In situ* data revealed a strong positive correlation between the presence of liquid water in the snow matrix and *in situ* T_B in the 37 and 89 GHz frequencies. When considering T_B ratios utilized by popular sea ice concentration algorithms (e.g., NASA Team 2), liquid water presence in the snow matrix was shown to increase the *in situ* T_B gradient ratio of 37/19V. *In situ* gradient ratios of 89/19V and 89/19H were shown to correlate positively with UAV-derived melt pond coverage across the ice surface. Multi-scale comparison between *in situ* T_B measurements and satellite-retrieved T_B (by Advanced Microwave Scanning Radiometer 2) showed a distinct pattern of passive microwave T_B signature at different stages of melt, confirmed by data from *in situ* thermophysical measurements. This pattern allowed for both *in situ* and satellite-retrieved T_B to be partitioned into three discrete stages of sea ice melt: late spring, early melt and advanced melt. The results of this study thus advance the goal of achieving more accurate modeled predictions of the sea ice cover during the critical navigation and breakup period in Hudson Bay.

Keywords: Sea ice; Passive microwave remote sensing; Unmanned aerial vehicle; Brightness temperature; Melt period; Hudson Bay

1 Introduction

Decline in the extent and concentration of Arctic sea ice has become a commonly used indicator of our rapidly changing climate (Peng and Meier, 2018). Sea ice extent and concentration decline are driven by the positive feedback loop of ice melt resulting from decreased ocean surface albedo (Perovich, 2002) and by external climatic responses such as deviations in atmospheric pressure patterns (Hochheim and Barber, 2010). High accuracy records of Arctic sea ice are vital for determining how these variables have changed historically in response to climate change, and for predicting how the Arctic Ocean system may evolve in the future.

Arctic sea ice extent and total concentration are calculated using sea ice concentration (SIC) algorithms (Kern et al., 2016). SIC algorithms predict ice concentration from satellite retrievals of microwave emissions from the Earth's surface. Using empirical knowledge of the microwave emissivity of various Earth surface types, algorithms have been generated to estimate the fractional coverage of surface types contributing to a single satellite measurement (Comiso et al., 1997; Hwang et al., 2007). This calculation is accurate during the winter, when emissions from the dry ice surface and ocean are distinct and well understood. The average accuracy of commonly used SIC algorithms in the winter is reported to be within ±5% in areas of high ice concentration (Ivanova et al., 2015).

* Centre for Earth Observation Science, Department of Environment and Geography, University of Manitoba, Winnipeg, Manitoba, CA

† Department of Electrical and Computer Engineering, University of Manitoba, Winnipeg, Manitoba, CA

Corresponding author: Madison L. Harasyn (madison.harasyn@umanitoba.ca)

Algorithm estimates become less reliable throughout the melt period as liquid water begins to persist on the ice surface, in the form of water suspended in the snow matrix or as melt ponds, rendering a microwave signature that deviates from the well understood winter sea ice signature (Onstott et al., 1987). The penetration depth of microwave frequencies in liquid water is on the order of millimeters (Ulaby and Long, 2014), preventing underlying ice emissions from reaching satellite sensors and rendering ponded melt water and open ocean to appear radiometrically similar. This effect decreases the accuracy of SIC estimates to values around ±20% at the summer ice edge (Ivanova et al., 2015), with some algorithms underestimating SIC up to 30% in ponded ice areas (Rösel et al., 2012b).

Several SIC algorithms have been developed to utilize different combinations of passive microwave frequencies and polarizations, such as NASA Team 2 (NT2; Markus and Cavalieri, 2000), Advanced Microwave Scanning Radiometer – Earth Observing System (AMSR-E) Bootstrap (Comiso, 2009), and Arctic radiation and turbulence interaction study (ARTIST) sea ice (ASI; Kaleschke et al., 2001; Spreen et al., 2008). These algorithms either directly compare raw passive microwave brightness temperature (T_B) at different frequencies to estimate SIC (e.g., Comiso, 2009) or use polarization ratios (PR) and gradient ratios (GR) to convert T_B into an intercomparable ratio between two polarizations or frequencies, respectively (e.g., Ivanova et al., 2015). The use of these ratios for SIC estimates is based on the frequency and polarization dependence of microwave emissivity across sea ice and open ocean (**Figure 1** in Comiso et al., 1997). The present study adopts these ratios as a way to compare *in situ* passive microwave measurements of known sea ice surface properties throughout the melt period to thresholds specified by SIC algorithms, in

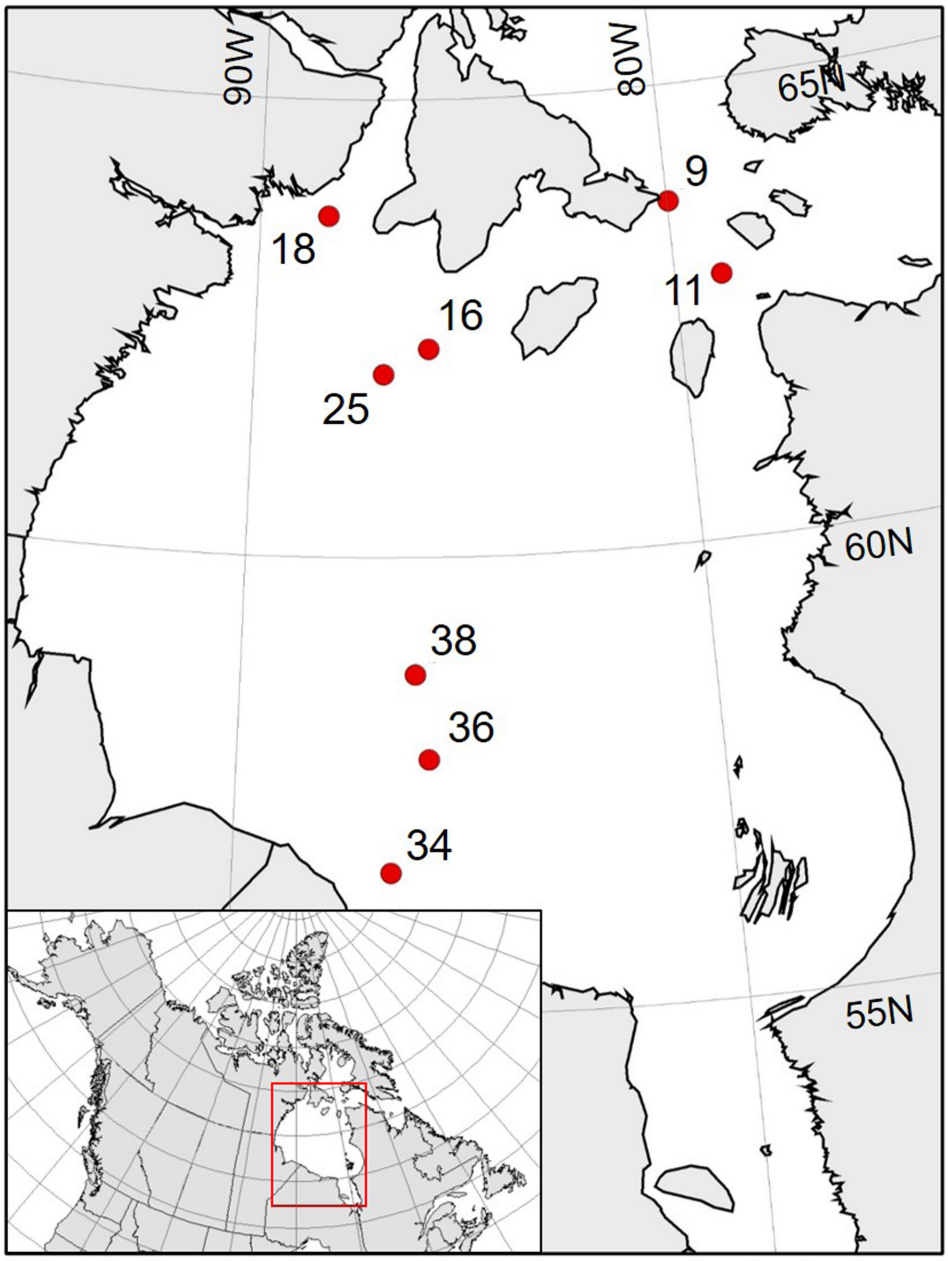

Figure 1: Location of sample sites across Hudson Bay in June 2018. Station numbers reflect the navigational path of the ship. Stage of melt increased as station number increased and the ship moved from north to south within the Bay. DOI: https://doi.org/10.1525/elementa.412.f1

order to assess how melt characteristics are expressed in SIC algorithms.

Previous research has compared *in situ* passive microwave T_B to satellite-based T_B as a way to assess remote retrievals of sea ice or snow properties (Hwang et al., 2007; Derksen et al., 2012). These types of analyses are limited by the spatial extent of satellite-based passive microwave pixels and the timing of satellite overpasses. For example, the Advanced Microwave Scanning Radiometer 2 (AMSR2) has a spatial resolution ranging from 5 km × 3 km (89.0 GHz) to 62 km × 35 km (6.93 GHz) and generates products twice daily for high latitudes (Du et al., 2014). As capturing an *in situ* measurement representative of a full satellite-based radiometer pixel is not possible logistically, interpolative methods must be adopted to facilitate this comparison. Herein, we use a multi-sensor approach, combining both optical and radiometric data to address spatial resolution issues in satellite-based radiometry. Methods are modelled from Kern et al. (2016), who use a combination of optical satellite imagery, satellite-retrieved passive microwave T_B and SIC products to assess the impact of melt ponds on satellite-based SIC retrievals.

This research addresses the following goals: 1) to describe the co-evolution of *in situ* passive microwave signatures and sea ice thermophysical properties throughout the melt period in Hudson Bay; 2) to determine if *in situ* observations of T_B can be compared meaningfully to satellite-retrieved T_B through a multi-sensor approach; and 3) to describe the co-evolution of remotely detected T_B, *in situ* T_B, and sea ice thermophysical properties throughout the melt period. In addressing these goals, we determine if physical relationships derived between sea ice surface properties and T_B are intercomparable between different spatial scales of measurement. This research combines *in situ* passive microwave measurements, thermophysical sea ice data, and UAV optical imagery stations to derive a small-scale relationship between progression of ice melt and T_B. *In situ* T_B is then compared to AMSR2-retrieved T_B, using optical Moderate Resolution Spectroradiometer (MODIS) imagery, ASI SIC products, and NT2 SIC products to facilitate scaling between spatial resolutions.

2 Methods

2.1 Hudson Bay ice climatology/rationale

Hudson Bay is a large inland sea that experiences a full melt and refreeze of sea ice during the annual cycle, resulting in the Bay being comprised predominantly of first year sea ice during the winter (Hochheim and Barber, 2014). The seasonality of sea ice is changing in Hudson Bay, with ice breakup occurring earlier and freeze-up occurring later in the year (Hochheim and Barber, 2014; Bliss et al., 2019). Various studies have assessed the change in the timing of sea ice formation/breakup (Gough et al., 2004; Gagnon and Gough, 2005; Hochheim and Barber, 2014; Bliss et al., 2019), being a metric of particular importance to shipping and maritime activities within the bay (Andrews et al., 2017). Despite Hudson Bay being an area of importance to the livelihoods of local communities, and a potential major shipping and tourism route for the Canadian prairie provinces (Dawson et al., 2016), few studies examining the passive microwave signature of Hudson Bay sea ice exist, particularly during the summer melt period.

2.2 Field methods

2.2.1 *In situ* station selection

Data were collected while on board the CCGS *Amundsen* icebreaker at various sites across Hudson Bay, Canada, from 3 June to 23 June 2018 as part of the Hudson Bay System Study (BaySys). Sample locations were chosen based on the navigational path of the ship (**Figure 1**), traveling from the northern section of the Bay towards the southern section throughout this time. The sampling period spanned across early to advanced ice melt in Hudson Bay, allowing for sample locations to be representative of a variety of ice conditions: early melt ice pack, ice edge, fragmented ice and advanced melt. As a result, a north to south gradient of stage of ice melt was sampled, with northern sites representing early melt and southern sites representing late melt.

2.2.2 *In situ* data collection

For each ice station, *in situ* radiometric data, ice thermophysical property data, and UAV station data (**Figure 2**) were collected for the same ice floe, undisturbed by the ship's transit. Ice floes selected for sampling were chosen by the team of scientific leads, ensuring that they were suitable for physical sampling and were representative of the general ice conditions in the area.

In situ passive microwave data were collected using a surface-based radiometer (SBR) mounted on the side of the ship approximately 12 m above sea level. The sea ice area in view of the SBR was chosen randomly based on the navigation of the captain, meaning that features within the field of view (FOV) of the SBR could not be controlled (e.g., melt pond coverage). The system consists of three dual-polarized antennas, collecting data at 19, 37 and 89 GHz in both the vertical and horizontal polarizations. Internal sensitivities of 0.04 K (19 GHz), 0.03 K (37 GHz) and 0.08 K (89 GHz) are reported in the manufacturer's specifications (Radiometrics, 2004). The system also housed an optical camera, capturing images of the general FOV of the SBR. Before data collection at each station, radiometric measurements were made of a cold source (clear sky) and a hot source (ECCOSORB® high loss microwave absorbing pad) following methods from Asmus and Grant (1999). These data were used to complete a two-point data verification to validate internal radiometer calibration. The SBR was set to collect data at 55°, corresponding to the incidence angle used in satellite T_B retrievals. Calculation of the area corresponding to the SBR FOV is presented in Section 2.2.1.

Thermophysical ice surface properties were sampled following radiometric data collection within the FOV of the SBR. Measurements were taken at three locations within the FOV, chosen to be representative of the whole ice surface within the FOV, ensuring that areas near ice ridges and melt ponds were included in sampling. Temperature, salinity, snow depth, snow grain size, and snow wetness were measured throughout the snow profile (**Table 1**, **Figure 3**). Temperature and salinity measurements were collected for the full ice profile, excluding station 34 where only the top 1 m of ice was sampled due to ice

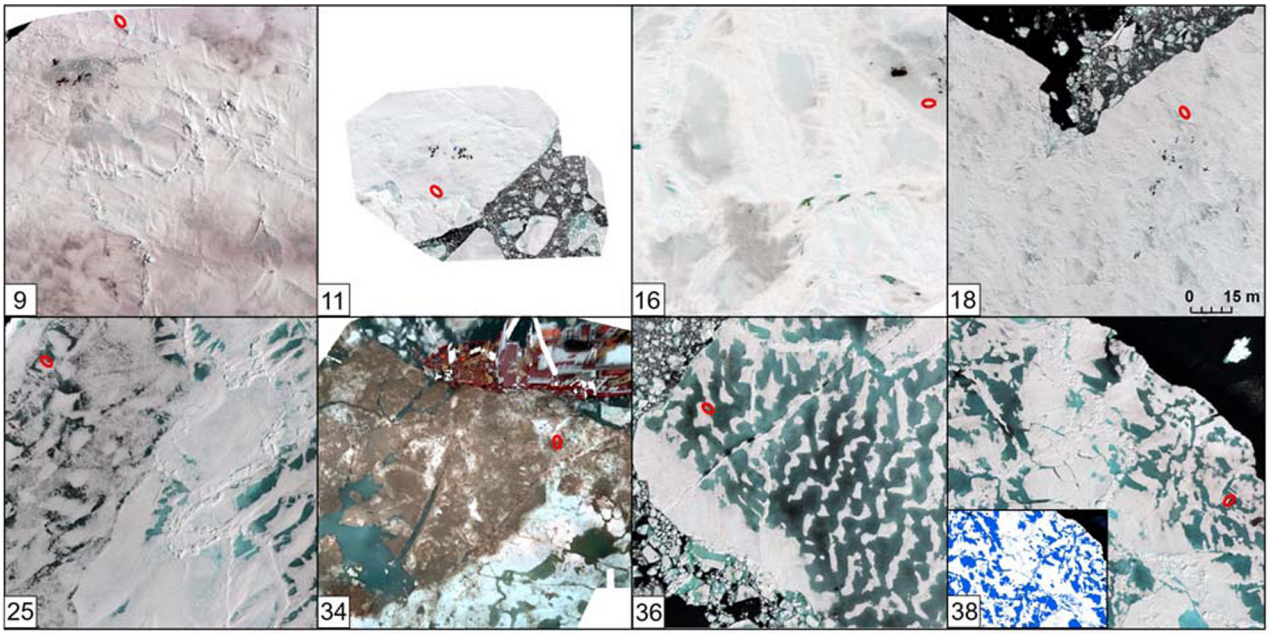

Figure 2: Unmanned aerial vehicle mosaics at each station showing stage of melt across each sampled floe. Red ovals represent the field of view of the surface-based radiometer. Subset image shows the output from melt pond classification for station 38, with blue representing melt ponds, white representing ice, and black representing ocean. Station number provided in bottom left corner. DOI: https://doi.org/10.1525/elementa.412.f2

Table 1: Parameters pertaining to physical sampling conducted at each station. DOI: https://doi.org/10.1525/elementa.412.t1

Parameter	Station							
	9	11	16	18	25	34	36	38
Sample date (2018)	03 June	04 June	06 June	08 June	13 June	21 June	22 June	23 June
Sample time (local EST, UTC-6)	09:03:57	13:19:37	10:59:58	13:20:43	08:34:39	12:32:51	08:24:38	10:46:07
Air temperature (°C)	–0.6	1.5	–0.6	3.2	1.7	5.8	1.5	6.8
Average snow depth (cm)	20	24	10	6	5	1	3	3
Mid-profile snow temperature (°C)	–2	–0.7	–0.5	0.4	0	0	0	0
Snow grain size (mm)	2	N/A[a]	3	3	N/A	3	3	3
Liquid present in snow matrix	Yes, slush at snow/ice interface, top 10 cm dry	Yes, slush at snow/ice interface, top 18 cm wet	No	Yes	No	Yes	Yes	Yes
Cloud cover (%)	0	90	100	0	0	50	90	10
Melt pond state within SBR FOV	No ponds	No ponds	No ponds	No liquid, 1-mm ice layer over 5-cm air pocket	Liquid pond covered with ≥2 cm of ice	Liquid, sediment-laden	Liquid pond covered with 0.5 cm of ice	Liquid pond covered with ~1 cm of ice

[a] Not available.

thickness exceeding the maximum thickness possible to sample with the provided ice-coring equipment, and to restrictions on time allocated to ice sampling at this location (**Figure 3**). Temperatures were measured on site, and ice cores were sectioned and melted for salinity measurements on board.

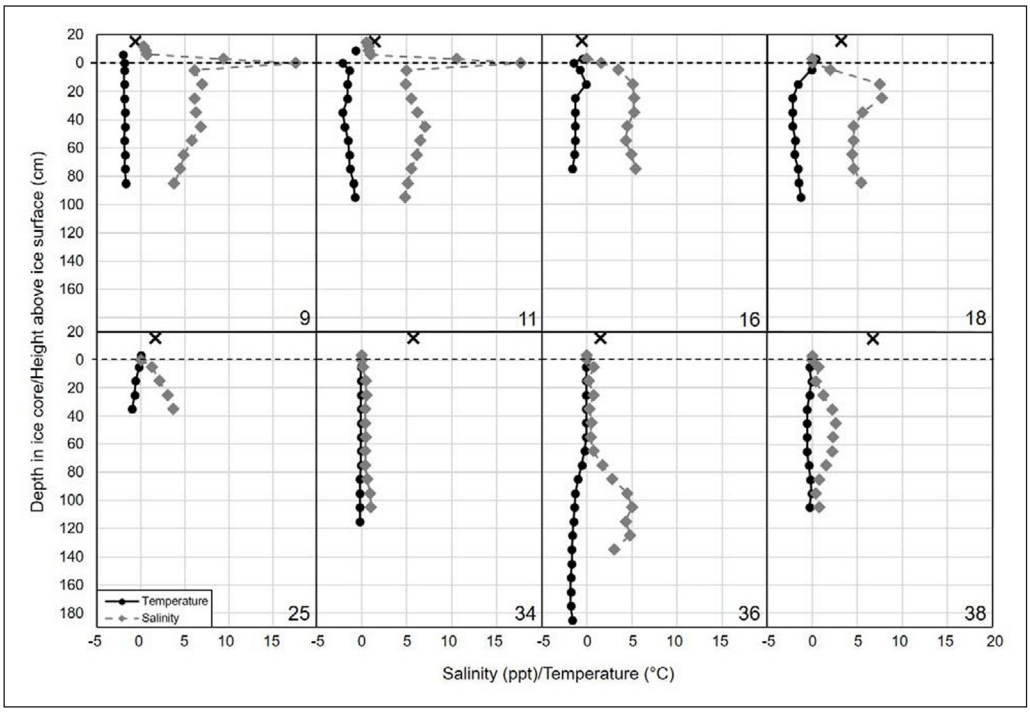

Figure 3: Vertical profiles for temperature and salinity at each ice station. Values for temperature (black circles) and salinity (grey diamonds) are displayed for snow at depths above 0 m (ice surface, dashed line) and for ice at depths below 0 m; a black X indicates air temperature. Station number provided in lower right corner. DOI: https://doi.org/10.1525/elementa.412.f3

Observations of SIC were recorded by the navigational crew of the *Amundsen* Coast Guard, who visually inspected the ice surrounding the ship during time of sampling. Recorded observations were converted to SIC percentage based on the extensive experience of the *Amundsen* captain and crew in conducting scientific missions in ice-covered waters. The spatial scale of these *in situ* SIC observations is approximately a 1-km radius around the ship.

UAV data were collected to determine total melt pond coverage across each sampled ice floe. Data were collected using a DJI Phantom 4 Pro quadcopter, equipped with 20 MP optical camera payload. A DJI Mavic Air quadcopter equipped with a 12 MP optical camera payload was used for station 34 due to limited sampling time. Flight surveys were pre-programmed using Map Pilot for DJI (©2019 Drones Made Easy, www.dronesmadeeasy.com/Articles.asp?ID=254), in a gridded flight path over the sampled floe. Surveys were captured at an altitude of 60 m to prevent interference from the ship's radar system on communication between the ground station and UAV. Due to the limited flight time and uniqueness of ice surface topography at station 34, the UAV survey was captured at an altitude of 20 m over a smaller area. UAV flight paths were programmed to ensure an along-track and across-track overlap of 70% to allow for the generation of optical orthomosaics. The GPSs onboard the DJI Phantom 4 Pro and Mavic rely on satellite positioning (GNSS) from GPS and GLONASS, having a reported global accuracy of approximately 0.1 m vertically and 1.5 m horizontally for absolute positioning (www.dji.com/ca/phantom-4-pro/info). Spatial coverage of UAV surveys was limited by the battery flight time, with DJI Phantom 4 Pro surveys being approximately 0.12 km^2 and the DJI Mavic Air survey being 0.013 km^2.

2.3 SBR data processing

2.3.1 Initial processing

T_B measurements collected for each sampled floe were averaged over the period where the FOV of the SBR fell within the extent of the physical sampling area. Averaged values represent from 3 to 8 measurements, depending on the amount of time the ship remained still. Measurements made at a stable location over the ice floe were selected using optical imagery captured coincident with T_B measurements from the camera housed in the SBR system.

The FOV of the SBR was calculated based on the approximate height of the SBR above the sea ice surface (12 m), the antenna half power beam width (6°), and the incidence angle of measurement (55°). The area of the SBR FOVs varied based on the frequency of measurement, ranging in area from 6.36 m^2 (89 GHz) to 6.62 m^2 (19 GHz) for a 55° incidence angle at a 12-m height. The overlap between FOVs is substantial (similar to **Figure 4** in Comiso et al., 1989); therefore, for simplicity in this analysis, the SBR FOV was calculated based on antenna half power beam width of the 19 GHz frequency, representing the largest FOV of measurement. Dimensions of the FOV with these specifications is 3.84 m by 2.19 m. This area was plotted on UAV imagery in ArcGIS Desktop 10.5 (ESRI, 2016) to calculate the fraction of melt ponds within the FOV of the SBR (**Figure 2**).

2.3.2 Polarization/gradient ratio calculations

We used PR and GR for direct comparison of T_B measured in the field to SIC algorithm tie points. The PR and GR for *in situ* T_B were calculated for frequency combinations used by SIC algorithms (Cavalieri et al., 1990; Markus and Cavalieri, 2000; Comiso, 2009). They include PR(19),

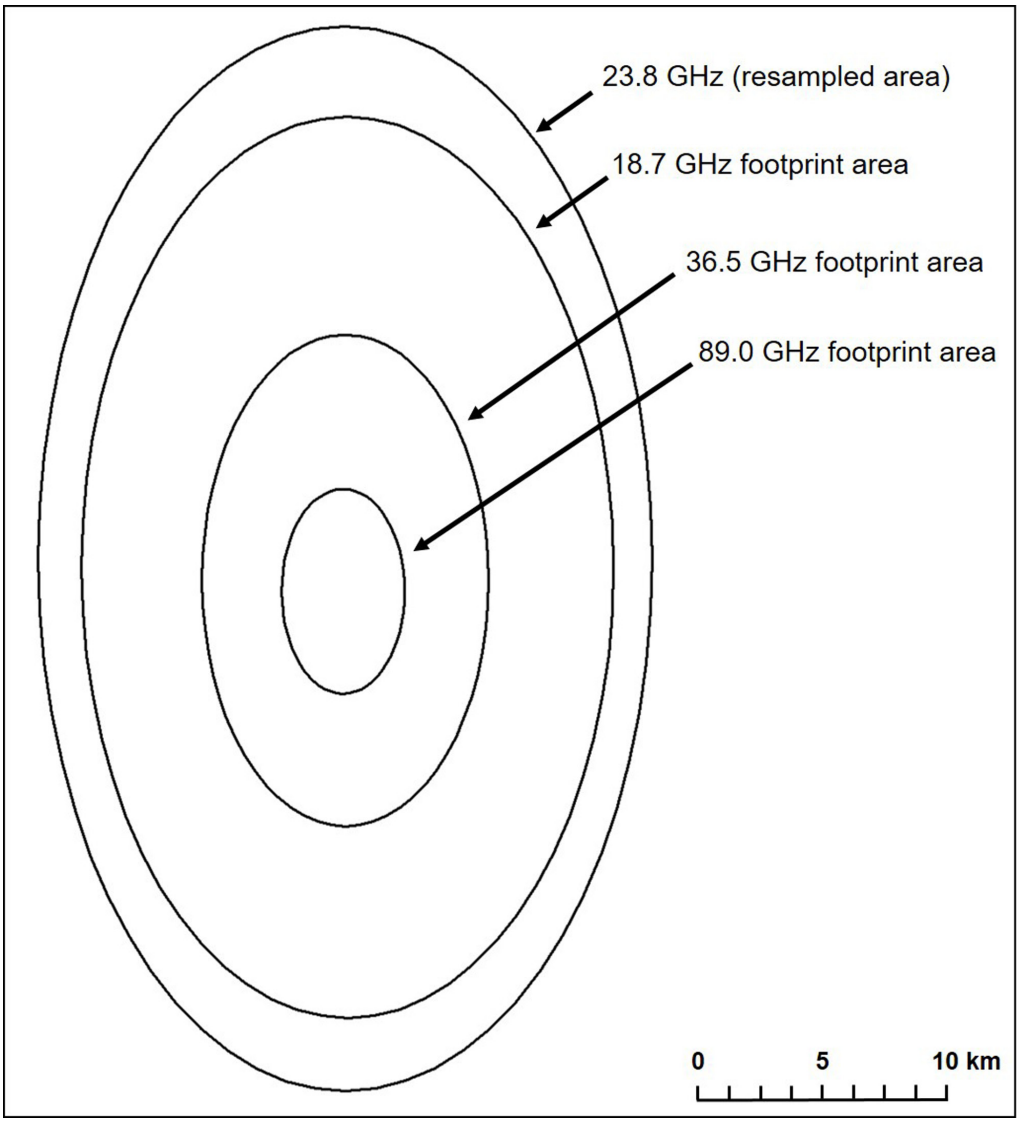

Figure 4: Schematic of AMSR2 footprint at different frequencies. The extent of the resampled area (23.8 GHz) is shown in comparison to the footprint areas of the three frequencies used in this analysis, for visualization of the differences in scale of data collection. DOI: https://doi.org/10.1525/elementa.412.f4

GR(37/19V), GR(89/19H) and GR(89/19V). The PR and GR were calculated as follows:

$$PR(f_1V) = \frac{T_B(f_1V) - T_B(f_1H)}{T_B(f_1V) + T_B(f_1H)} \quad (1)$$

$$GR(f_1V/f_2V) = \frac{T_B(f_1V) - T_B(f_2V)}{T_B(f_1V) + T_B(f_2V)} \quad (2)$$

where f_1 and f_2 correspond to the one or two frequency channels of interest, and V and H represent measurements in the vertical and horizontal polarizations, respectively (Comiso et al., 1997).

2.4 UAV imagery processing

2.4.1 Initial processing

UAV image sets for each station were processed using Pix4D® image processing software (www.pix4d.com). Images were stitched based on geolocation to generate a single optical orthomosaic of the sampled floe and surrounding area. Spatial resolution of UAV orthomosaics are approximately 2.5 cm for all image sets collected with the Phantom 4 Pro, whereas the Mavic Air image set has a spatial resolution of 7 mm resulting from the low flying altitude.

2.4.2 Image classification

To describe the stage of melt of the sampled ice floe, total melt pond coverage was determined using a supervised classification for the full extent of each optical orthomosaic. Melt pond, ice, and open ocean classes were generated following methods from Rösel et al. (2012a) and Toyota et al. (2010), based on the reflectance of these three surfaces in the red (600 nm), green (540 nm) and blue (460 nm) channels captured by UAV imagery (example subset in **Figure 2**). This classification method assumes UAV imagery contains pure pixels, with only one class type within each pixel. Two classification signatures were generated to effectively classify optical imagery captured at

stations experiencing early melt (Table A1) versus late melt (Table A2). This step was to avoid melt pond areas being overestimated for station areas experiencing early-stage melt (stations 9, 11, 16 and 18), such as shadow areas or areas of slight snow discoloration. As station 34 contained a high sediment concentration on the ice surface, melt ponds were classified using a unique spectral signature following methods outlined in Harasyn et al. (2019).

The ratio of melt pond area to total ice surface area for the full extent of the floe, and within the area of the SBR FOV, was determined based on UAV image georectification. Areal fraction estimates of open ocean or ice floe sizes were not determined, as the total UAV coverage area was not uniform between stations, making this metric inadequate for station comparisons.

2.5 Satellite-based remote sensing data

2.5.1 Radiometric satellite data

Temporally and spatially coincident satellite-based radiometric data were retrieved for all sample locations (**Table 2**). The date and time of satellite data acquisition closest to the time of *in situ* radiometric data collection was chosen, falling within 4.5 hours of each other. Radiometric satellite data were retrieved from the Advanced Microwave Scanning Radiometer 2 (AMSR2) sensor, with data being obtained from the Japan Aeronautics Exploration Agency (JAXA) G-Portal website (gportal.jaxa.jp). Level-1R T_B data were retrieved for 18.7, 36.5 and 89.0 GHz (simplified to 19, 37 and 89 GHz hereinafter), resampled to the spatial resolution of the 23.8 GHz sensor, for comparison with *in situ* data. Level-1R data resamples T_B to a common resolution across frequencies, allowing for the calculation of frequency ratios which are commonly used in geophysical parameter algorithms (Du et al., 2014; Karvonen, 2014; Lavergne et al., 2019). The native resolution of each frequency is as follows: 19 GHz = 14 × 22 km, 37 GHz = 7 × 12 km and 89 GHz = 3 × 5 km (**Figure 4**). The resampled resolution of the data is 15 × 26 km, meaning resampled T_B for 37 GHz and 89 GHz is averaged over many data points, whereas 19 GHz T_B data is close to the native resolution. Further information on methods of data resampling can be found in Data User's Manual for AMSR2 Products produced by JAXA (JAXA, 2013). T_B for 19, 37 and 89 GHz for both polarizations were extracted for the AMSR2 pixel coinciding with each sample location.

Table 2: Time (UTC) of in situ passive microwave (PMW) measurements and AMSR2 and MODIS image collection at each station. DOI: https://doi.org/10.1525/elementa.412.t2

Station #	Date	*In situ* PMW	AMSR2	MODIS (Aqua)
9	3 June	13:03:57	17:19	08:30
11	4 June	17:19:37	16:24	07:35
16	6 June	14:59:58	17:50	18:40
18	8 June	17:20:43	17:38	18:25
25	13 June	12:34:39	08:09	18:45
34	21 June	16:32:51	17:07	08:20
36	22 June	12:24:38	08:47	18:35
38	23 June	14:46:07	16:55	08:05

2.5.2 Optical satellite data

Optical satellite data were retrieved to provide a sense of large-scale ice and atmospheric conditions within the FOV of the AMSR2 sensor. Optical imagery was obtained from the Moderate Resolution Imaging Spectroradiometer (MODIS)/Aqua (250 m resolution), with data being obtained from the NASA Worldview Data Explorer website (worldview.earthdata.nasa.gov). Time of MODIS data capture is not temporally coincident with *in situ* passive microwave measurements, sometimes falling ~10 hours apart and on average 6 hours of one another (**Table 2**). MODIS imagery is thus not representative of the exact sea ice and atmospheric conditions during time of collection; however, these data provide a general sense of conditions impacting AMSR2 T_B retrievals.

MODIS imagery was collected by selecting a 100 km by 100 km area surrounding the *in situ* sample location coordinates on Worldview Data Explorer and downloading the image as a .geotif file format. Georectified satellite data rasters were then imported into ArcGIS Desktop 10.5 (ESRI, 2016) for data analysis. An oval representing the footprint of the resampled AMSR2 data (15 km × 26 km) containing each *in situ* station location was overlain on MODIS imagery, providing moderate-resolution imagery of the ice and atmospheric conditions within the pixel area (**Figure 5**). From MODIS imagery, the influence of cloud cover and approximate sea ice concentration/surface conditions on AMSR2 T_B could be estimated for each station.

2.5.3 Satellite-based SIC products

AMSR2 ASI SIC v5.4 product (Spreen et al., 2008) and NT2 daily average SIC (Markus and Cavalieri, 2000) were retrieved to estimate the SIC within the AMSR2 pixel area of interest. These two products were chosen as they calculate SIC using the same frequencies corresponding to *in situ* measurements, and they represent a high resolution (ASI) and low resolution (NT2) SIC grid. ASI SIC products are generated once daily, whereas NT2 SIC products are generated twice daily. As a result, we chose the NT2 daily average SIC product for this research to allow for comparison with the ASI product. SIC products corresponding to the date of AMSR2 T_B data collection were chosen (**Table 2**).

AMSR2 ASI SIC utilizes T_B measured at 89 GHz V-pol and H-pol to resample SIC down to 3.125 km grid resolution for the Arctic3125 product which is used in this analysis (Spreen et al., 2008). The AMSR2 ASI SIC algorithm utilizes the polarization difference between 89 GHz V-pol and H-pol to estimate the total SIC within a pixel area (Spreen et al., 2008). The use of higher frequency channels allows for a finer spatial scale of SIC products (3.125 × 3.125 km); however, higher frequencies are more sensitive to atmospheric water vapor which causes SIC overestimation. To address this issue, ASI has a built-in weather filter based on GR(36.5/18.7V) and GR(23.8/18.7V) (Spreen et

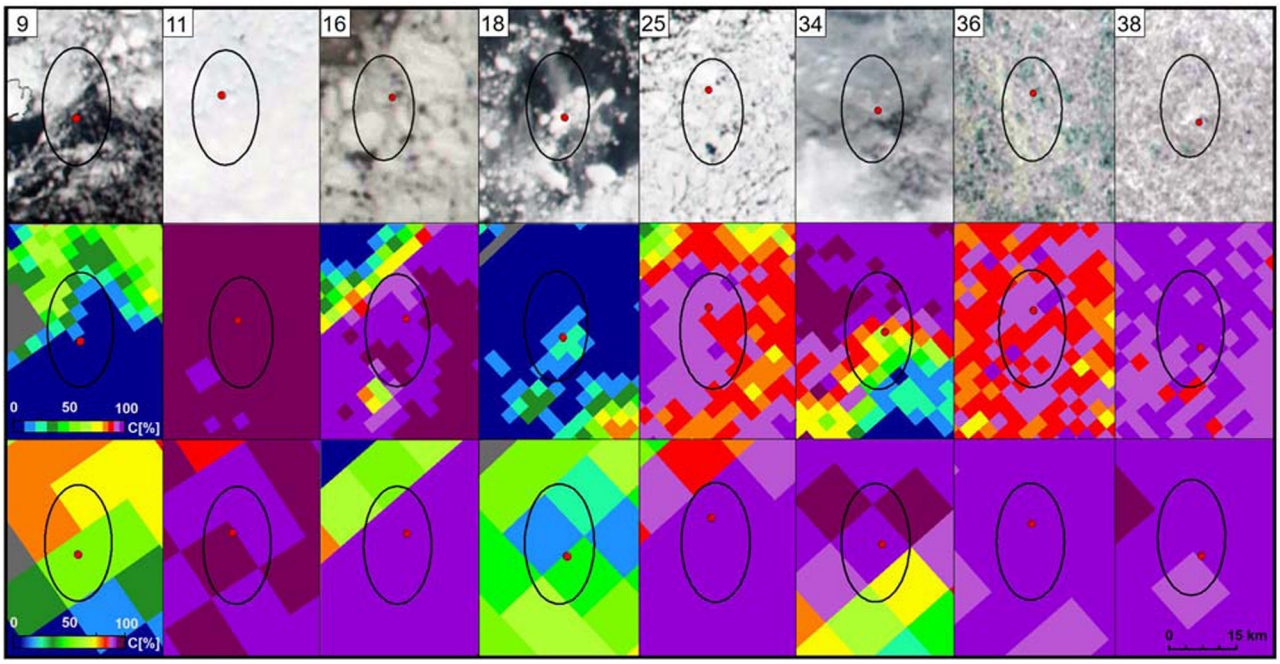

Figure 5: MODIS imagery (top), ASI SIC (middle) and NT2 SIC (bottom) corresponding to each station. AMSR2 resampled footprint extent (black oval, representing 15 km × 26 km) is overlain on each satellite product, with the *in situ* sampling location displayed as a red dot. Land represented in grey for SIC products. Station number provided in upper left corner. DOI: https://doi.org/10.1525/elementa.412.f5

al., 2008). This filter does not impact the spatial resolution of the SIC product; however, it is expected to cause an overestimation of SIC along the ice edge. Data were downloaded from the Institute of Environmental Physics, University of Bremen, Germany (seaice.uni-bremen.de/sea-ice-concentration/).

NT2 SIC uses T_B measured at 19, 37 and 89 GHz in a series of T_B ratios (PR, GR) to determine SIC. The NT2 algorithm is based on the original NASA Team algorithm, calculating SIC based on known emissive values of FYI, MYI and OW across different frequencies, also known as tie points (Cavalieri et al., 1984; Markus and Cavalieri, 2000; Meier et al., 2017). T_B ratios used in this algorithm are as follows: PR(19), GR(37/19V), GR(89/19H) and GR(89/19V) (Meier et al., 2017). Weather filters are applied in the algorithm to account for the effects of atmospheric water vapour on the 89 GHz frequency. Thresholds are defined based on the GR of retrieved T_B, and atmospheric conditions within the pixel are estimated based on the calculated GR from a look-up table of 12 pre-defined atmospheric profiles (Meier et al., 2017). To account for sea ice surface effects, the enhanced NT2 introduces the use of ΔGR (the difference between GR(89/19H) and (89/19V); Markus and Cavalieri, 2000; Meier et al., 2017). Surface effects, such as surface glazing or layering, lead to increased PR(19) values and cause an underestimation of SIC (Matzler et al., 1984). The NT2 addresses these surface refreezing effects through the implementation of ΔGR; however, surface effects from melt processes are not addressed through the inclusion of this term (Meier et al., 2017). SIC is calculated at a 12.5 km grid resolution. Data were downloaded from the National Snow and Ice Data Center (https://nsidc.org/data/AU_SI12/versions/1; Meier et al., 2018).

The location of *in situ* sampling and the representative footprint of the resampled AMSR2 data were overlain on the corresponding ASI and NT2 (**Figure 5**) SIC product to allow for comparison of these datasets. From this comparison, the ASI and NT2 SIC surrounding each station can be determined.

3 Results

3.1 In situ *station description*

3.1.1 Sea ice thermophysical properties

Temperature and salinity profiles throughout the snow and ice show the progression of melt with increasing station number (**Figure 3**). The thermophysical properties measured on the ice surface agree with this trend as well (**Table 1**). As station number increases, sea ice surface temperatures and salinities progress towards 0 due to ice surface warming and drainage of brine. All stations have a near-isothermal temperature profile, indicating that all stations were near or experiencing ice melt (**Figure 3**). Stations also progress from having a thick snow layer and no melt ponds to a thin snow layer with extensive melt ponding (**Table 2**, **Figure 2**). This progression indicates that a representative set of ice conditions throughout the melt period were captured in this dataset.

Stations 9 and 11 had a snowpack with a low salinity at the air-snow interface (~1 ppt), rapidly increasing to a salinity of ~17 ppt at the snow-ice interface (**Figure 3**) which was noted in the field to be a layer of highly saturated slush. This layer of high snow salinity could result from saline waters of Hudson Strait being washed onto the ice surface, influenced by currents bringing saline water into the Bay from the Labrador Sea (Hochheim and Barber, 2014). These stations also had the thickest layer

of snow on the ice surface (~20 cm) with no melt ponds present on the surface (**Table 1**, **Figure 2**).

Station 18 appears to be at an intermediate stage of melt, having a wet snow layer of 6 cm and areas that appear to be melt ponds in aerial imagery (**Figure 2**); however, physical sampling revealed that these areas consisted of a layer of ice above approximately 1 cm of air (**Table 1**). The ice salinity profile suggests that the top layers of the ice were beginning to drain, as there is a steep increase of salinity midway through the ice profile (**Figure 3**). The ice temperature profile suggests that only the top 10 cm was actively experiencing ice melt, as underlying layers had temperatures around −2°C (**Figure 3**).

Stations 34, 36 and 38 were all experiencing advanced melt conditions, having temperatures above −1°C for the top 60 cm of ice, ice surface salinities of ~0 ppt, and snow temperatures of 0°C, with liquid water present throughout the snowpack (**Figure 3**, **Table 1**). These stations also exhibit extensive melt ponding across the surface (**Figure 2**), with stations 36 and 38 being affected by potential diurnal refreezing of the top 0.5–1 cm of melt ponds (**Table 1**).

Stations 16 and 25 are the only stations with a completely dry snowpack on the ice surface (**Table 1**). Both stations had snow and ice surface salinities of 0 ppt, with salinity increasing with depth through the ice (**Figure 3**). These two stations do appear to be at different stages of melt, as station 25 had melt ponds and a thinner snow layer whereas station 16 had a thicker snow layer and no melt ponds. Melt ponds at station 25 were covered with a thick (>2 cm) ice layer, which may be related to the time of sampling (08:34), causing diurnal refreezing of liquid water. Despite these features, liquid water was not present in the snow matrix at time of sampling; therefore, these two stations can be expected to be radiometrically similar, in comparison to other stations.

Varying surface properties were measured within the FOV of the SBR (**Table 1**). At stations 9 through 18, the SBR collected measurements of a relatively smooth ice surface free of melt ponds. Station 25 includes a portion of a melt pond in the FOV; however, this melt pond was measured to have a 2-cm-thick layer of ice on the surface. Stations 34 through 38 include a large portion of melt pond within the FOV; however, each melt pond was unique: station 34 contained open liquid water, station 36 was covered with 0.5 cm of ice, and station 38 was covered with 1 cm of ice.

3.1.2 UAV-derived melt pond coverage

Melt pond fraction (MPF) shows an overall trend of increase with increasing station number, representing sampling dates further into the melt season (**Table 3**). Station 11 appears to be an outlier, having an MPF greater than 10% compared to the remaining early melt sites. During the time of sampling, station 11 had an air temperature above 0°C and a wet snowpack with a saturated basal layer (**Table 1**), which could have influenced initial melt pond formation.

Table 3: Fraction of the full sampled floe covered by melt ponds (melt pond fraction, MPF), and MPF within the field of vision (FOV) of the surface-based radiometer (SBR), determined from supervised classification of UAV imagery. DOI: https://doi.org/10.1525/elementa.412.t3

Station #	MPF (%)	
	Full floe	within SBR FOV
9	0.4	0
11	13.2	0
16	0.7	0
18	1.9	0
25	19.9	45.7
34	32.2	12.0
36	44.8	76.5
38	30.8	94.9

3.2 In situ *data inter-comparison*

3.2.1 Thermophysical properties versus *in situ* T_B

The passive microwave signature for each station is unique; however, some similarities can be found between certain stations (**Figure 6a**). Stations 16 and 25 have very similar passive microwave signatures, with linearly decreasing T_B with increased frequency for both polarizations. Stations 11, 34 and 38 have T_B for all frequencies around 250 K, with T_B for both polarizations in the same frequency being equal or near-equal (excluding station 34, 34 GHz).

Pearson's correlation coefficient was calculated for each physical variable and T_B polarization/frequency combination to assess the influence of thermophysical properties on *in situ* T_B signature (**Table 4**). A point-biserial correlation statistic was calculated between wetness and T_B due to the binary nature of the wetness variable. A bivariate statistical analysis was chosen over a multivariate analysis due to the small sample size of the data (8 stations) (de Winter, 2013). Snow grain size was omitted during this analysis due to missing data for some stations, and as grain size remained similar throughout data collection (**Table 1**).

Overall, *in situ* T_B values do not appear to show a strong correlation with cloud cover at time of measurement, snow depth or snow temperature in this dataset (**Table 4**). The majority of sampled snow matrices contained liquid water, however, which greatly influences the passive microwave signature of the ice, potentially influencing the correlation between measured snow variables and T_B.

Hour of sampling shows a positive correlation (0.89, $p = 0.00$) with *in situ* T_B at 19 GHz V-pol, meaning that T_B increased for sampling conducted later in the day (**Table 4**). At 19 GHz H-pol a positive correlation is also observed between *in situ* T_B and hour of sampling (0.74), but the relationship is not statistically significant ($p = 0.35$). Air temperature also has a positive correlation (0.75, $p = 0.03$) with *in situ* T_B at 89 H-pol (**Table 4**). The majority of p-values in this analysis are too high for the relationships to be statistically significant. A larger dataset

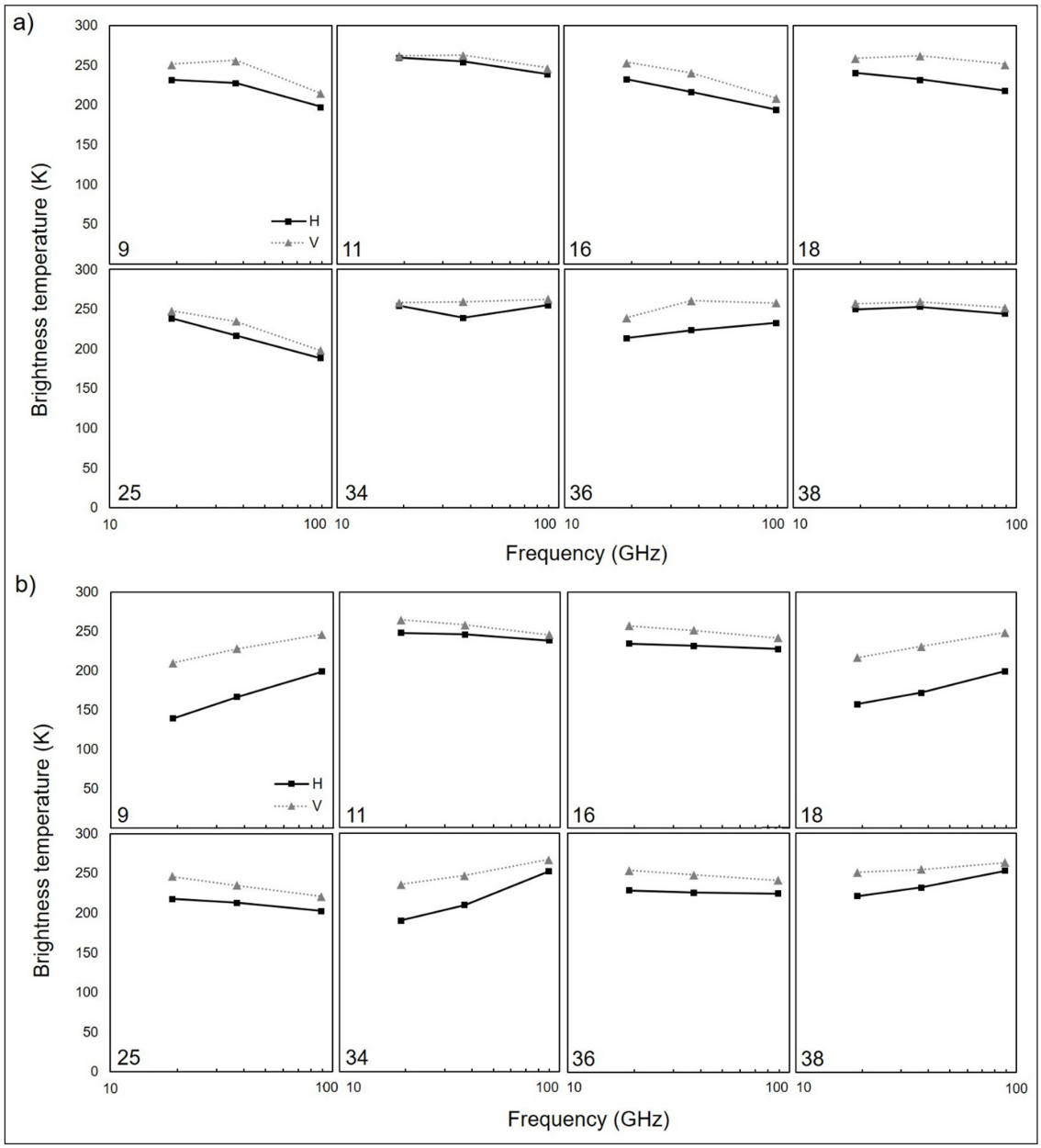

Figure 6: T_B profiles across increasing measurement frequency for all stations. Graphs represent **a)** *in situ* T_B and **b)** temporally coincident AMSR2 T_B. Station number provided in the lower left corner. DOI: https://doi.org/10.1525/elementa.412.f6

Table 4: Pearson's correlation coefficients calculated between thermophysical variables and T_B for each frequency/polarization channel. DOI: https://doi.org/10.1525/elementa.412.t4

Frequency/ polarization	Correlation coefficients[a]					
	Wetness[b]	Percent cloud cover	Hour of sampling	Air temperature	Snow depth	Snow temperature
19 H	0.1859	–0.1222 (0.89)[b]	0.7411 (0.35)	0.5173 (0.19)	0.2238 (0.59)	0.0815 (0.85)
19 V	0.2212	–0.0969 (0.93)	0.8853 (0.00)*	0.3575 (0.38)	0.3256 (0.43)	0.0083 (0.98)
37 H	0.6271	–0.0025 (0.38)	0.6204 (0.10)	0.6057 (0.11)	0.239 (0.57)	0.0364 (0.93)
37 V	0.9066	0.0707 (0.65)	0.5017 (0.21)	0.3921 (0.34)	0.1449 (0.73)	0.0029 (0.99)
89 H	0.6837	0.231 (0.24)	0.5196 (0.19)	0.7502 (0.03)*	–0.2301 (0.58)	0.3456 (0.40)
89 V	0.7644	0.1891 (0.40)	0.5163 (0.19)	0.6575 (0.08)	–0.2852 (0.49)	0.4203 (0.30)

[a] P values shown in parentheses; asterisks indicate statistically significant (95% confidence interval) coefficients.
[b] Calculated using point-biserial correlation.

could allow for a stronger correlation to be observed between these environmental variables and T_B.

Snowpack wetness has a positive correlation with 37 GHz (H-pol: 0.63, V-pol: 0.91) and 89 GHz (H-pol: 0.768 V-pol: 0.76) T_B in both polarizations (**Table 4**). As a result of the binary nature of the wetness variable, the particular relationship expressed in this analysis is that liquid water presence in the snow matrix leads to higher 37 GHz and 89 GHz T_B, in comparison to snow matrices without liquid water. T_B at 19 GHz does not show a strong correlation with snowpack wetness in either polarization.

3.2.2 Thermophysical properties versus *in situ* SBR T_B PR/GR

Following Markus and Cavalieri (2000) *in situ* SBR T_B values for all stations for PR(19) and GR(37/19V) were plotted against one another, creating a feature space scatterplot (**Figure 7**). Tie points associated with the NT2 algorithm (Markus and Cavalieri, 2000) were plotted within the scatterplot referencing the clear sky tie point for open water (OW), first year ice (FYI) and multi-year ice (MYI) (**Figure 1b** in Markus and Cavalieri, 2000).

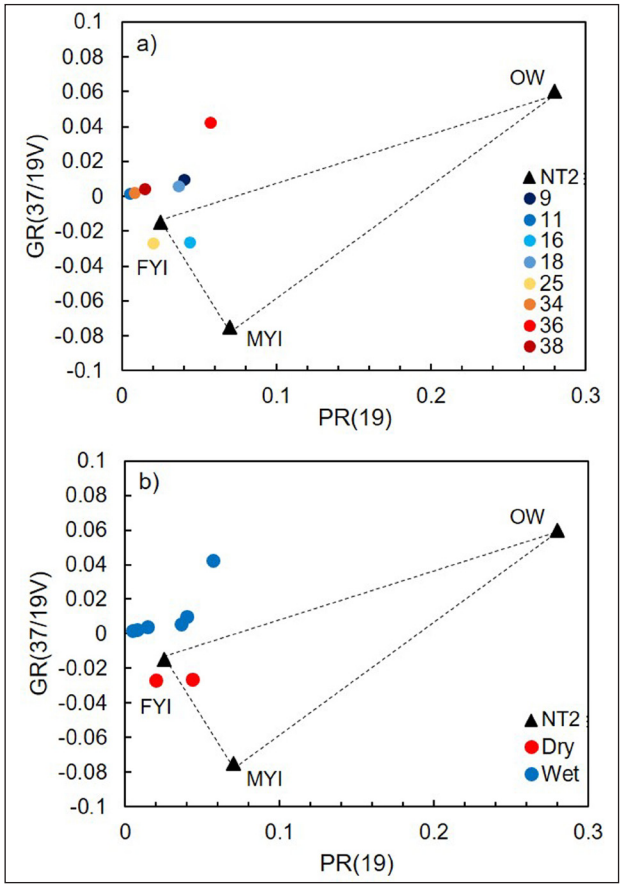

Figure 7: *In situ* T_B plotted in parameter space against tie points specified for the NT2 algorithm. Graphs represent GR(37/19V) vs PR(19) labeled by **a)** station number and **b)** based on the presence or absence of liquid water on the ice surface, in the form of liquid water in the snow matrix or melt ponds not impacted by surface refreezing (linear distance between *in situ* SBR T_B and NT2 tie points provided in Table 5). DOI: https://doi.org/10.1525/elementa.412.f7

Tie points for clear sky conditions were chosen, as *in situ* measurements of T_B are impacted minimally by atmospheric effects due to the small distance between the sensor and observed area (~21 m for this experiment), in comparison to satellite-based sensors. This approach allowed for the assessment of the proximity of *in situ* SBR T_B values to SIC algorithm tie points.

Upon first assessment of *in situ* SBR T_B values in the parameter space of **Figure 7a**, all station values fall in proximity to the 100% FYI tie point. The majority of stations have a GR(37/19V) T_B greater than FYI, with station 36 having a GR(37/19V) value much greater than the FYI tie point. Station 36 also falls the closest to the OW tie point along the GR(37/19V) axis (**Table 5**), suggesting that this site may have been under greater influence of surficial liquid water content in comparison to the remaining stations. Stations 16 and 25 are the only stations having GR(37/19V) values lower than the FYI tie point. These stations also happen to be the only stations with no liquid water present within the snow matrix during sampling. When represented as 'wet' (liquid water present in snow matrix) or 'dry' (no liquid water in snow matrix) sites within the scatterplot feature space, the separability of these stations is emphasized (**Figure 7b**). Stations with a dry snow matrix have a GR(37/19V) T_B below –0.02, whereas all stations with liquid water present in the snow matrix have a GR(37/19V) value above 0.

3.2.3 SBR T_B versus UAV-derived MPF

The relationship between MPF and *in situ* SBR T_B was assessed on the basis of MPF being an indicator of the progression of ice surface melt. Upon first assessment, raw *in situ* SBR T_B values are not linearly related to melt pond coverage. For further comparison, the PR and GR of *in situ* SBR T_B reported in the previous section were compared to MPF. Overall, *in situ* PR and GR are not correlated to melt pond coverage across the full floe or within the FOV when stations with a dry snow matrix (sta-

Table 5: Linear distance between *in situ* SBR T_B and NT2 tie points within PR(19) vs GR(37/19V) feature space corresponding to Figure 7a. DOI: https://doi.org/10.1525/elementa.412.t5

Station #	Linear distance[a]	
	OW	FYI
9	0.25	0.03
11	0.28	0.03
16	0.25	0.02
18	0.25	0.02
24	0.28	0.04
25	0.27	0.01
34	0.28	0.02
36	0.22	0.07
38	0.27	0.02

[a] To tie point for open water (OW) or first year ice (FYI).

Table 6: Pearson's correlation coefficients between *in situ* surface-based radiometry (SBR) gradient ratios (GR) and melt pond fraction (MPF), corresponding to Figure 8. DOI: https://doi.org/10.1525/elementa.412.t6

Gradient ratio	Full floe MPF		MPF within the SBR FOV	
	Including dry stations	Including dry stations	Excluding dry stations	Excluding dry stations
GR(37/19V)	0.526 (0.18)	0.349 (0.40)[a]	0.487 (0.22)	0.554 (0.15)
GR(89/19H)	0.765 (0.03)*	0.470 (0.24)	0.687 (0.06)	0.967 (0.00)*
GR(89/19V)	0.673 (0.07)	0.373 (0.36)	0.559 (0.15)	0.848 (0.01)*

[a] P values shown in parentheses, with statistically significant (95% confidence interval) coefficients indicated by asterisk.

tions 16 and 25) are included (**Table 6**). When these stations are excluded, a moderate positive correlation exists between GR(89/19H) and MPF within the SBR FOV, having a Pearson's correlation coefficient of 0.69 (p = 0.06) (**Figure 8a**). This relationship is weakened by station 38, which has the highest MPF within the FOV yet GR values similar to stations with an MPF of 0 (**Figure 8a**). This case is a result of the 1-cm-thick ice covering melt ponds at this station (**Table 1**), making melt ponds appear as smooth ice radiometrically. A positive correlation exists between full floe MPF and GR(89/19H) as well as GR(89/19V) (**Figure 8b**). Both gradient ratios have a positive correlation with MPF, with GR(89/19H) having a Pearson's correlation coefficient of 0.97 (p = 0.00) and GR(89/19V) having a correlation of 0.85 (p = 0.01) (**Table 6**).

High correlation between GR and full floe MPF, in comparison to MPF within the SBR FOV, may be related to the relationship between full floe MPF and state of surface melt in this dataset. For example, station 38 has the highest MPF within the SBR FOV, whereas station 36 has the highest full floe MPF (**Table 3**). Physical sampling data show that melt ponds at station 38 were covered with 1-cm-thick ice, whereas station 36 melt ponds were covered with 0.5 cm ice (**Table 1**). As a result, the radiometric signature for station 36 will be more affected by melt processes, whereas the radiometric signature of melt ponds at station 38 would be blocked by ice formation, hence the differences seen between **Figure 8a** and **8b**.

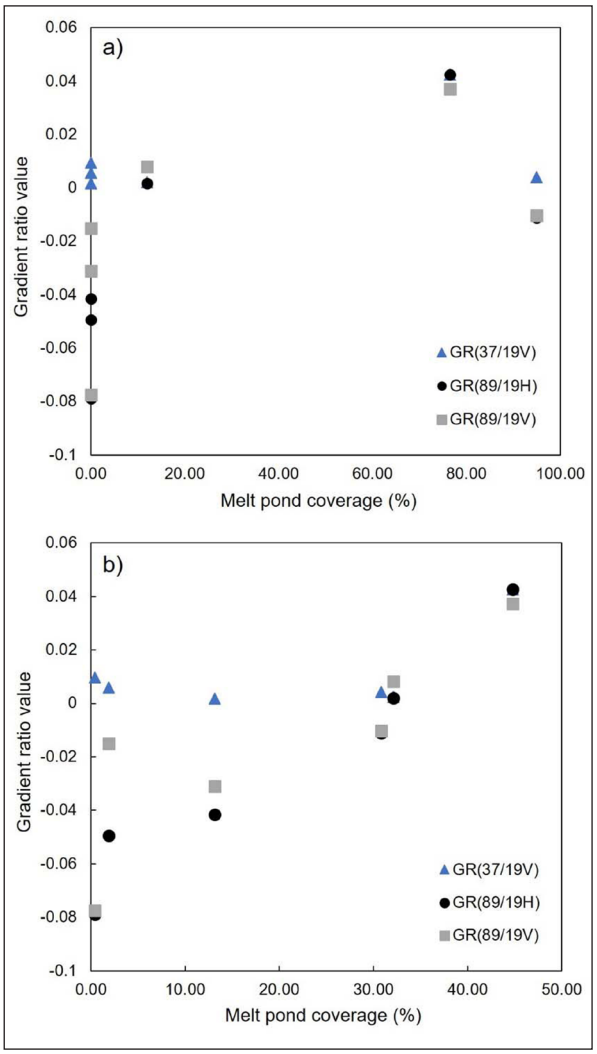

Figure 8: *In situ* gradient ratio versus melt pond coverage for surveys having a wet snow matrix. GR is shown for **a)** melt pond coverage within the FOV of the SBR, and **b)** melt pond coverage for the full floe sampled. Strong statistical relationships are not evident between GR and melt pond coverage within the SBR FOV, but a strong positive linear relationship exists between GR(89/19H) and full floe melt pond coverage (statistics provided in Table 6). DOI: https://doi.org/10.1525/elementa.412.f8

3.3 Comparison of in situ *data and satellite-retrieved data*

3.3.1 *In situ* SIC observations versus satellite-derived SIC products

To determine the effects of open water on AMSR2-retrieved T_B, we considered two commonly used SIC products: ASI and NT2. Satellite-based SIC products were used to extrapolate *in situ* bridge-observed SIC over a larger area, allowing for a more representative indication of open water percent within each ASMR2 pixel extent. In the following paragraphs, we compare these products to observed *in situ* SIC surrounding the ship at the time of data collection to determine the variability of SIC observations/products over different spatial scales, in order to provide an estimate of the total SIC contributing to ASMR2-retrieved T_B.

Comparing satellite-derived SIC values surrounding each station for the ASI and NT2 algorithm (**Table 7**, **Figure 5**) indicates that these algorithms agree relatively well. Stations within the ice pack (stations 11, 16, 25, 36 and 38) agree between ASI and NT2 SIC (**Figure 5**). For stations along the ice edge, ASI SIC agrees with bridge-observed *in situ* SIC for stations 9 and 34, whereas NT2 SIC and *in situ* SIC agree best for station 18. Stations 9, 18

and 34 are all along the ice edge, leading to incongruency between *in situ* observations and algorithm SIC estimates.

For quantitative comparison, correlation coefficients were calculated between the bridge-observed *in situ* SIC and both the ASI and NT2 SIC to determine the similarity between these SIC observation/measurement scales. Correlation between ASI SIC and NT2 SIC is high (0.97, p = 0.00), showing that both algorithms are producing similar results during this period. Both SIC products agree well with bridge-observed *in situ* SIC; however, the correlation between ASI and *in situ* SIC (0.96, p = 0.00) is higher than the correlation between NT2 and *in situ* SIC (0.93, p = 0.00). This higher correlation is related to the similarity of spatial scale of *in situ* SIC observations (radius of ~1 km) and ASI SIC (3.25 km), in comparison to NT2 SIC (12.5 km).

To determine if ASI and NT2 SIC products are intercomparable on a similar spatial scale, an aggregate raster of ASI SIC was created by calculating the mean of all ASI SIC gridded values falling within each NT2 grid spaces (**Table 8**). The minimum, maximum, and standard deviation of ASI SIC values within the aggregated grid space of 12.5 km × 12.5 km vary between stations. Stations with more uniform values across the minimum, maximum, mean and standard deviation SIC values include stations 11, 16, 25, 36 and 38 which are within the ice pack and station 9 which is proximal to a large area of open ocean (**Table 8**). Stations 18 and 34 have varying SIC statistics, and are proximal to the ice edge (**Table 8**). These differences can be observed in the spatial distribution of SIC in **Figure 5**.

After ASI product aggregation, the correlation value between *in situ* SIC and ASI SIC decreased to 0.93 (p = 0.00), equal to the correlation between *in situ* SIC and NT2 SIC. Interestingly, ASI pixel aggregation reduced the correlation between NT2 SIC and ASI SIC from 0.97 to 0.95 (p = 0.00). This reduction means that pixel aggregation of a higher resolution SIC product does not necessarily make SIC values more comparable to a lower resolution product. However, all modes of SIC observation/calculation produced similar results to a statistically significant correlation (correlation > 0.9, $p < 0.05$); therefore, both products can be used with confidence to assess total SIC contributing to AMSR2 T_B.

Table 7: Bridge-observed *in situ* sea ice concentration (SIC) at each station, and satellite-derived SIC from ASI and NT2 products. DOI: https://doi.org/10.1525/elementa.412.t7

Station #	SIC (%)		
	In situ	NT2	ASI
9	20	57	0
11	90	100	100
16	90	99	91
18	30	43	9
25	70	97	92
34	50	78	61
36	80	95	90
38	90	94	96

3.3.2 Direct comparison of *in situ* T_B and satellite-retrieved AMSR2 T_B

In situ T_B was plotted against coinciding AMSR2 T_B for direct comparison (**Figure 9**). Overall, V-pol T_B is clustered within the range of 200–260 K along both axes, whereas H-pol experiences more outliers, particularly along the AMSR-2 T_B axis. Values for 89 GHz V-pol and H-pol fall closest along the 1:1 slope, meaning that *in situ* T_B and AMSR2 T_B are most similar for measurements at 89 GHz. Values for 19 and 37 GHz H-pol have outliers with low AMSR2 T_B in comparison to *in situ* values. These three outliers correspond to stations 9, 18 and 34 (stations with the lowest AMSR2 T_B in **Figure 9**).

Pearson's correlation coefficient was calculated between *in situ* T_B and coincident AMSR2 T_B for each station, considering the full suite of all frequency/polarization combinations for each platform of measurement for correlation analysis (**Table 9**). Stations 11, 16 and 25 have the highest correlation between *in situ* T_B and AMSR2 T_B (0.84, 0.83 and 0.78, respectively), with stations 11 and 16 having a statistically significant p-value (p = 0.04). Correlation was also calculated between *in situ* T_B and coincident AMSR2

Table 8: Pixel statistics calculated for ASI sea ice concentration (SIC) after pixel aggregation to a resolution of 12.5 km × 12.5 km, corresponding to NT2 SIC resolution. DOI: https://doi.org/10.1525/elementa.412.t8

Station #	NT2 SIC (%)	ASI aggregate SIC			
		Mean (%)	Max (%)	Min (%)	Standard deviation (%)
9	57	1	15	0	3.74
11	100	100	100	100	0
16	99	97	100	91	3.27
18	43	13	25	3	7.89
25	97	90	94	84	2.74
34	78	82	98	46	14.49
36	95	90	97	84	3.29
38	94	94	98	92	1.86

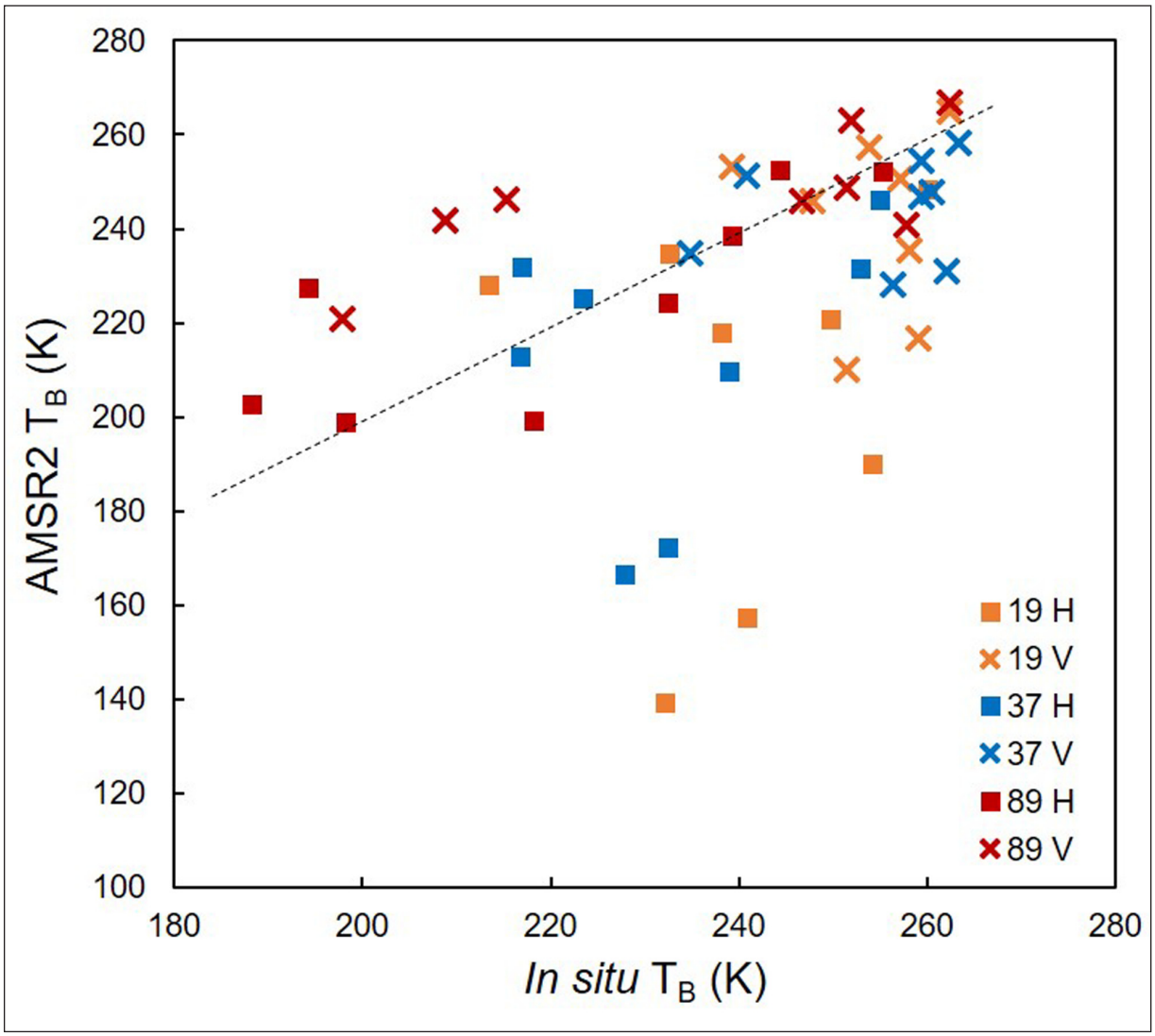

Figure 9: *In situ* T_B versus AMSR2-retrieved T_B for spatially and near-temporally coincident measurements. Absolute agreement (1 to 1 correlation) between *in situ* T_B and AMSR2 T_B is shown as a dashed line. DOI: https://doi.org/10.1525/elementa.412.f9

Table 9: Pearson's correlation between *in situ* T_B and AMSR2 T_B for each station. DOI: https://doi.org/10.1525/elementa.412.t9

Station #	Coefficient	P-value
9	0.061	0.91
11	0.842*	0.04
16	0.829*	0.04
18	0.560	0.25
25	0.782	0.07
34	0.620	0.19
36	0.690	0.13
38	0.187	0.72

* Indicates statically significant coefficients (95% interval).

T_B by frequency/polarization of measurement (**Table 10**). Values for 89 GHz H-pol and V-pol show strong correlations (0.79 and 0.73, respectively), both having p-values <0.05.

Table 10: Pearson's correlation between *in situ* T_B and AMSR2 T_B for each frequency/polarization channel. DOI: https://doi.org/10.1525/elementa.412.t10

Frequency/polarization	Coefficient	P-value
19 H	0.108	0.80
19 V	0.045	0.92
38 H	0.308	0.46
37 V	0.197	0.64
89 H	0.789*	0.02
89 V	0.730*	0.04

* Indicates statically significant coefficients (95% interval).

3.4 In situ *T_B versus satellite-retrieved T_B using a multi-sensor approach*

3.4.1 Assessment of the impact of atmospheric effects and low SIC on satellite-retrieved T_B

Comparing *in situ* T_B with satellite-retrieved T_B is inherently difficult, due to the large difference in spatial scale of these two modes of data collection. In this research, *in*

situ T_B was collected for a 3.84 m by 2.19 m elliptical area, for which the position of the FOV can be controlled so that the T_B measurement consists of 100% ice. Resampled AMSR2 T_B data used for this study has a spatial resolution of 15 km by 26 km, often capturing a mixture of sea ice and ocean within one pixel area. When comparing T_B measurements across these two scales of measurement, two major considerations must be addressed: the concentration of ice within the extent of an AMSR2 pixel, and the atmospheric effects on higher frequency microwave measurements (89 GHz). *In situ* SIC observations and SIC products from ASI and NT2 were used to estimate the total ice concentration contributing to AMSR2 retrieved T_B. To address atmospheric effects, cloud cover conditions recorded during *in situ* sampling and from MODIS imagery were taken into consideration (**Table 1**, **Figure 5**). Atmospheric effects minimally impact *in situ* T_B in comparison to satellite-retrieved T_B, due to the minimal distance that the emissions travel through the atmosphere to reach the *in situ* sensor. For this comparison the thermophysical properties of sea ice within the extent of an AMSR2 pixel are assumed to be uniform, as the field sampling schedule did not permit the collection of sea ice thermophysical measurements for multiple stations within a pixel area.

To address these considerations, we use a combination of datasets as a way to facilitate the comparison between *in situ* T_B and satellite-retrieved T_B. A combination of *in situ* SIC and algorithm-derived SIC is used to provide an estimate of the total sea ice area contributing to satellite-retrieved T_B. Atmospheric effects on satellite-based T_B were determined through coincident MODIS imagery and *in situ* observations of cloud cover. By assessing how each coincident AMSR2 T_B measurement is influenced by SIC and atmospheric effects, these effects can be addressed, facilitating direct comparison between *in situ* T_B and AMSR2 T_B.

Directly comparing *in situ* T_B signatures to AMSR2 signatures (**Figure 6**) shows that stations 9 and 18 have the largest discrepancies. This result is attributed to these two stations being proximal to open water (**Figure 5**), making the AMSR2 T_B signatures resemble open water as opposed to the signature measured *in situ* (**Figure 6b**). Station 34 also has an AMSR2 T_B signature deviant from *in situ* values. Station 34 has SIC ranging from 50 to 78% (**Table 7**), leading to low AMSR2 T_B at 19 and 37 GHz. Values for station 34 T_B at 89 GHz agree between AMSR2 and *in situ* values, resulting from the high native spatial resolution of the 89 GHz satellite sensor.

Next, we consider the effect of cloud presence on AMSR2-retrieved T_B determined from *in situ* observation and MODIS imagery. Stations 11, 16 and 36 have *in situ* cloud cover over 80%, and therefore AMSR2-retrieved values for T_B are likely affected by atmospheric water vapor. Considering MODIS imagery, stations 11, 16, 18 and 34 appear to be impacted by cloud cover (**Figure 5**). Stations 36 and 38 are within a dense ice pack, making MODIS imagery appear fully white, which makes interpreting cloud cover difficult (**Figure 5**); therefore, *in situ* values are used exclusively. High cloud cover is expected to increase T_B measured for 89 GHz, due to contributions of microwave emissions from atmospheric water vapor. Station 16 has the largest discrepancy between *in situ* and AMSR2 T_B values at 89 GHz, with AMSR2 T_B values being ~35 K higher than *in situ* values (**Figure 6**). AMSR2 T_B values for the remaining frequencies are also higher compared to *in* situ values for station 16: 37 GHz values are ~10 K higher, and 19 GHz values are ~2 K higher. These discrepancies fall within discrepancies between *in situ* and AMSR2 T_B calculated for other stations; however, station 16 is the only location where AMSR2 T_B values for all frequencies are greater than *in situ* values (**Figure 6**). Station 16 also has the highest cloud cover, measured *in situ* to be 100%. This relationship between cloud cover, *in situ* T_B, and AMSR2 T_B is not expressed in data for stations 11 and 36, as these stations both have 90% cloud cover yet T_B values for AMSR2 89 GHz are lower than *in situ* values (**Figure 6b**). From these findings, we conclude that atmospheric water vapor must be above a particular threshold before satellite-retrieved T_B for 89 GHz is greatly impacted.

This analysis has allowed for the identification of data points affected by high cloud cover or low SIC, which therefore have been removed for the final comparison between *in situ* T_B and satellite-retrieved AMSR2 T_B. The stations that remain for this comparison are stations 11, 25, 36 and 38.

3.4.2 Comparison of *in situ* T_B and satellite-retrieved T_B throughout the melt period

To determine if the evolution of T_B signature over the melt period is similar over different scales of measurement, *in situ* T_B and remotely-sensed T_B are directly compared throughout the melt season across the remaining stations not impacted by low SIC or atmospheric effects (stations 11, 25, 36 and 38; **Figure 10**). Three stages of the melt period are captured by these stations based on *in situ* thermophysical properties. Station 25 is classified as 'late spring', as it had a dry ice surface, likely due to diurnal refreezing, radiometrically similar to late spring sea ice. Station 11 had a wet snowpack but minimal melt pond formation, representing 'early melt'. Stations 36 and 38 are classified as 'advanced melt' given a melt pond coverage >30% (**Table 3**).

Overall, T_B signature for late spring has lower *in situ* and AMSR2-retrieved T_B at each frequency compared to T_B values later in the melt season (**Figure 10**). Late spring T_B also shows a steady decrease in T_B with increased frequency for both polarizations. When water is introduced into the snow matrix during early melt, *in situ* and AMSR2 T_B increase for all frequencies (**Figure 10**). Early melt T_B values are on average 25 K greater than late spring T_B, demonstrating that liquid water in the snow pack greatly influences the satellite-based radiometric signature of sea ice. As well, PR and GR values for *in situ* T_B and AMSR2 T_B decrease for all frequencies between late spring and early melt (**Figure 10**).

Progressing from early melt to advanced melt, a general trend of decreasing 19 and 37 GHz T_B and increasing polarization ratio, particularly for 19 and 37 GHz, is seen for both scales of T_B (**Figure 10**). This trend is a result of the formation of melt ponds on the ice surface,

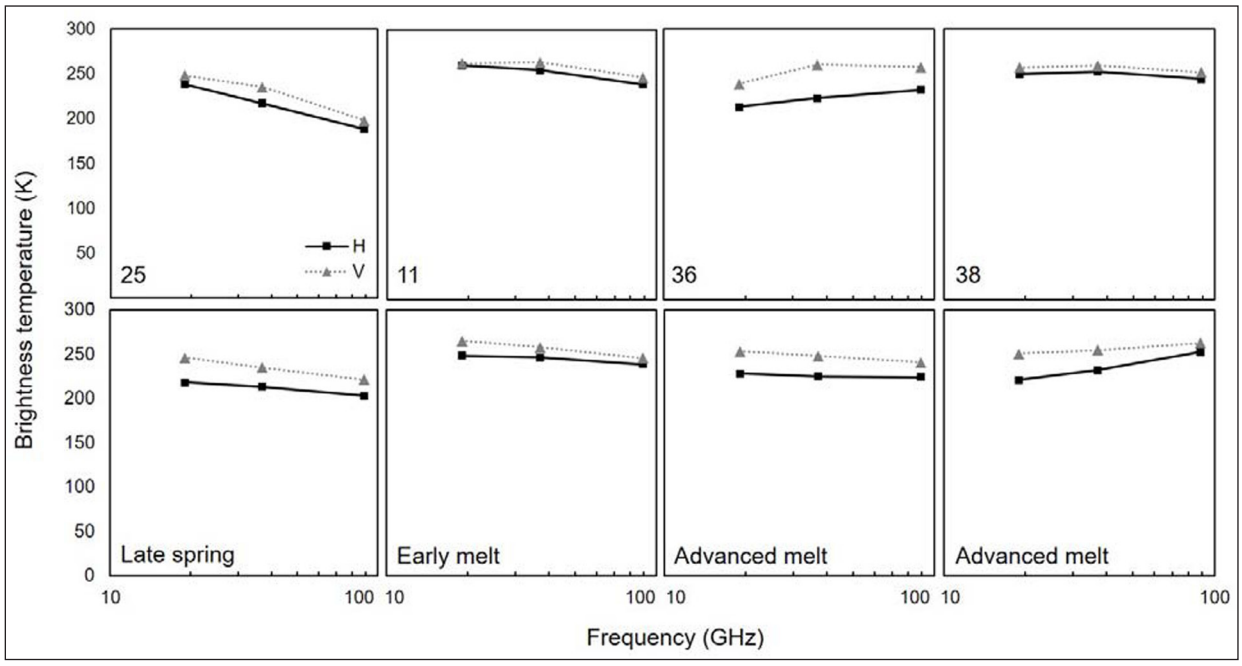

Figure 10: AMSR2-retrieved T_B signatures for selected stations not impacted by low SIC or atmospheric effects. A clear transition from a negative to positive relationship between T_B and frequency of measurement is seen from late spring to advanced melt. Station numbers left to right are: 25, 11, 36 and 38. DOI: https://doi.org/10.1525/elementa.412.f10

which would theoretically decrease satellite-retrieved T_B and increase the polarization in T_B (Ivanova et al., 2015). However, T_B for station 38 is dissimilar for *in situ* and AMSR2 T_B (**Figure 10**). *In situ* T_B for station 38 has a signature similar to early melt, whereas the ASMR2 T_B signature is more similar to advanced melt, excluding 89 GHz. *In situ* T_B signature of this station is influenced by the layer of thick (1 cm) ice on the surface of melt ponds at this station, resulting in a T_B signature similar to early melt. This effect is also seen in AMSR2 89 GHz T_B, which may be a result of the sensitivity of the high-resolution sensor to potentially local melt pond refreezing. This suggestion is a hypothesis, as the ice conditions surrounding each station were not measured.

4 Discussion

4.1 Thermophysical properties versus in situ *T_B*

Within the dataset of this study, *in situ* T_B did not correlate with snow depth or snow temperature. Previous studies have shown a relationship between snow depth and passive microwave signature (Grenfell, 1986; Markus et al., 2006; Rostosky et al., 2018); however, that relationship is based on a winter snow pack. The absence of correlation between T_B and snow depth in the present dataset is a result of the influence of liquid water in the snow pack on the measured passive microwave signature (Ulaby and Long, 2014; Rostosky et al., 2018).

Liquid water presence in the snow matrix and T_B for 37 GHz and 89 GHz were positively correlated in both polarizations (**Table 4**). Previous research has shown snow emissivity increases in all frequencies during melt onset, when liquid water content in the snow matrix exceeds winter values (Grenfell, 1986; Eppler et al., 1992). The exclusion of 19 GHz in this correlation can be explained by the change in sea ice surface emissivity between late spring and early summer (Onstott et al., 1987). Results from Onstott et al. (1987) show surface emissivity increases at higher frequencies between late spring and early summer, while emissivity at lower frequencies remain relatively similar (**Figure 7** in Onstott et al., 1987). Results from our data agree with this relationship: stations with a dry snow matrix are characteristic of the late spring microwave emission pattern, whereas those with a wet snow matrix are characteristic of the early to late summer emission pattern outlined in Onstott et al. (1987) (**Figure 6**).

4.2 Thermophysical properties versus in situ *SBR T_B PR/GR*

Overall, *in situ* PR(19) and GR(37/19V) values for all stations agree with the clear sky FYI tie point of the NT2 algorithm (**Figure 7a**). Stations with liquid water present in the snow pack have GR(37/19V) values consistently higher than the FYI tie point and PR(19) values evenly dispersed around the FYI tie point. Stations with and without liquid water present in the snow matrix can be identified easily within the feature space: stations with a wet snowpack have a GR(37/19V) greater than 0, and stations with a dry snowpack have a GR(37/19V) less than –0.02 (**Figure 7b**). As a result, we can conclude that liquid water presence in the snow matrix increases the GR(37/19V) but has no preferential effect on PR(19).

This conclusion agrees well with physical sampling results described in the previous section. Liquid water presence in the snow matrix was shown to correlate with an increase in T_B at higher frequencies, driving an increase in GR(37/19V) but having minimal effect on PR(19). This result is also in agreement with Grenfell (1986) and Onstott et al. (1987), who both show a more pronounced

increase in emissivity during early melt at higher frequencies in comparison to winter emissivity values.

4.3 SBR T_B versus UAV-derived MPF

Considering UAV MPF, the strongest correlations occur between full floe MPF and GR(89/19H) and GR(89/19V) (**Table 6**). Both gradient ratios increase from –0.08 to 0.04 as full floe melt pond coverage increases from 0 to 45% (**Figure 8b**). The strength of this correlation can be explained by the nature of our dataset, where stations with the highest full floe MPF are experiencing the most progressed stage of melt (i.e., thinner ice cover over melt ponds, shallower snow pack) (**Table 1**). The presence of a layer of freshwater ice over melt ponds produces a T_B signature where T_B increases with increased frequency (Ulaby and Long, 2014), which would generate an increase in GR values. In combination with this effect, Onstott et al. (1987) show that lower frequencies experience a decrease in T_B as melt progresses from early summer to late-summer. This progression is caused by a formation of subsurface and surface melt ponds as snow depth decreases due to melting (**Figure 6** in Onstott et al., 1987). Physical data from our stations agree with this progression of melt, as stations experienced both a decrease in snow depth (**Table 1**) and increase in melt pond coverage (**Table 3**) throughout the melt period. Therefore, the correlation between full floe MPF and GR(89/19V and H) expressed in our data is driven by a combination of melt pond surface freezing and increased liquid water in the snow matrix driving an increase in 89GHz T_B and a decrease in 19 GHz T_B.

4.4 In Situ *SIC observations versus satellite-derived SIC products*

To facilitate comparison between *in situ* T_B and AMSR2 T_B, *in situ* observed SIC was compared to algorithm-calculated ASI and NT2 SIC. Both algorithms agreed with *in situ* observations, with the ASI algorithm having the highest correlation with *in situ* observations due to its high spatial resolution. The following sections address how changes in the thermophysical properties of sea ice are predicted to affect SIC algorithm products, and if an effect is seen in our data.

4.4.1 *In situ* SIC observations versus NT2 SIC

Based on results outlined in the preceding sections, melt processes on the sea ice surface are expected to influence the NT2 algorithm in the following ways: liquid water presence causes an increase in GR(37/19V) through an increase in T_B for 37 and 89 GHz, and a decrease in 19 GHz T_B, between early to mid-summer. The ΔGR term in the NT2 algorithm is then expected to increase with an increase in melt pond coverage, leading to an underestimation in SIC. In contrast, NT2 SIC is consistently greater than *in situ* SIC and ASI SIC for all stations, including stations along the ice edge, with the majority of stations having an NT2 SIC 10% greater than *in situ* observations (**Table 7**). This may be related to processes outlined by Kern et al. (2016), who indicate that SIC algorithms experience overestimation when open water is present between melt-ponded ice floes.

Overall, the highest agreement between *in situ* SIC, ASI SIC and NT2 SIC is for stations surrounded by high SIC; i.e., stations 11 and 38 (**Table 7**). Both of these stations had liquid water present in the snow matrix and melt ponds present on the ice surface (**Tables 1** and **3**), which suggests that both algorithms account well for liquid water presence on the ice surface for areas within the ice pack. NT2 SIC has the highest discrepancy in comparison to *in situ* and ASI SIC for station 34 (**Table 7**). NT2 SIC would be expected to be lower than ASI SIC at this location, as the NT2 pixel extent contains the ice edge; however, NT2 SIC is greater than ASI SIC (**Figure 5**, **Table 7**). Station 34 is the only station without a layer of ice on the surface of melt ponds, and is located along the ice edge as shown by ASI SIC (**Figure 5**), which suggests that areas of ponded ice proximal to the ice edge may not be classified as well as areas of ponded ice within the ice pack.

4.4.2 *In situ* SIC observations versus ASI SIC

Considering the reliance of the ASI algorithm on the 89 GHz channel, stations experiencing high cloud cover are expected to have higher ASI SIC in comparison to *in situ* values. Stations with a high cloud cover include stations 11, 16, 18, 34, and 36, determined from *in situ* observations (**Table 1**) and MODIS imagery (**Figure 5**). Comparing *in situ* and ASI SIC values for these stations, ASI agrees very well with *in situ* values (**Table 7**). ASI overestimates SIC by 10% for stations 11 and 36, and underestimates SIC by 20% for station 18. These percentages fall within the overall discrepancy between *in situ* and ASI SIC for all stations, suggesting that the ASI weather filter accurately discerns microwave measurements originating from atmospheric water vapor and sea ice.

Stations proximal to the ice edge are also represented well by the ASI SIC product. Stations close to the ice edge include stations 9, 16, 18, 25 and 34, observed from MODIS imagery (**Figure 5**). *In situ* SIC agrees with ASI SIC for these stations, being both greater (stations 25 and 34) and lower (stations 9 and 18) than *in situ* SIC, as would be expected for SIC observations of different scales along the ice edge.

4.5 Co-evolution of in situ *T_B and satellite-retrieved T_B throughout the melt period*

Through a multi-sensor approach, *in situ* T_B and satellite-based T_B were successfully partitioned into three stages of sea ice melt based on T_B signature similarities found at both scales, using T_B signatures provided in Onstott et al. (1987). During late spring, T_B is lower compared to values later in the season and decreases with increasing frequency in both polarizations, for both *in situ* and satellite-retrieved T_B. In the early melt stage when liquid water is introduced into the snow matrix, *in situ* and satellite-retrieved T_B increases in all frequencies, and PR/GR values decrease. Advanced melt is marked by the formation of melt ponds on the ice surface, which drives a decrease in 19 and 37 GHz T_B and an increase in PR for 19 and 37 GHz. Formation of a thick layer (~1 cm) of ice on the surface of melt ponds results in the T_B signature of ice being similar to early melt, despite the ice having thermophysical characteristics resembling advanced melt.

Results from the comparison between *in situ* T_B and AMSR2-retrieved T_B agree with results presented in Section 3.2, relating to *in situ* T_B and thermophysical property analyses. At both scales of measurement, liquid water presence in the snow matrix during early melt was shown to increase T_B in all frequencies. This increase agrees with the comparison between *in situ* T_B and thermophysical properties reported in Section 4.1. In AMSR2 data, melt pond formation during advanced melt was shown to influence PR at lower frequencies (**Figure 10**). This phenomenon is similar to *in situ* data; however, thick ice cover on the melt pond surface masks the emission signature of liquid melt ponds, rendering a signature similar to early melt. Results reported in Section 4.2 show that melt ponds increase GR(89/19V) and GR(89/19H) (**Figure 8**), which agrees with both *in situ* T_B and AMSR2 T_B. Overall, relationships derived between sea ice thermophysical properties and *in situ* T_B agree with AMSR2 T_B, suggesting that *in situ* studies of T_B signatures can be scaled up effectively to satellite-retrieved T_B signatures.

5 Conclusion

This research has considered the *in situ* and satellite-based passive microwave T_B collected within Hudson Bay at various sea ice thermophysical stages throughout the melt period. Stations showed surface thermophysical properties corresponding to late spring, early melt and advanced melt, following the melt stage classification outlined in Onstott et al. (1987). Melt stage was determined through a combination of *in situ* thermophysical property sampling and UAV optical imagery collection.

Analysis of *in situ* T_B in relation to sea ice thermophysical properties revealed a strong positive correlation between liquid water presence in the snow matrix and *in situ* T_B for frequencies 37 and 89 GHz. *In situ* T_B for all stations agreed with PR(19) values for the NT2 clear sky FYI tie point. Stations where liquid water was present in the snow pack had GR(37/19V) values greater than the FYI tie point, whereas stations with a dry snow matrix were slightly lower than the NT2 FYI tie point. GR(89/19H) and GR(89/19V) were positively correlated with UAV-derived full floe melt pond coverage. Overall, liquid water presence in the snow pack and in melt ponds was shown to drive an increase in high frequency T_B (37 and 89 GHz) and a decrease in lower frequency T_B (19 GHz).

To facilitate with scaling discrepancies between *in situ* T_B and AMSR2-retrieved T_B, SIC products from two algorithms (NT2 and ASI) and cloud cover from MODIS imagery were retrieved. Stations experiencing low SIC or high cloud cover expressed the expected impacts in AMSR2 T_B, with low SIC leading to lower AMSR2 T_B in comparison to *in situ* T_B, and high cloud cover generating an increase in AMSR2 89 GHz T_B in comparison to *in situ* T_B.

Direct comparison of *in situ* and AMSR2 T_B by frequency showed that 89 GHz has the highest correlation between the two scales of measurement. Areas of low SIC were shown to have lower AMSR2 T_B for 37 and 19 GHz, but this decrease was not seen in 89 GHz T_B. This lack of decrease is likely a result of the high native resolution of the 89 GHz sensor, which is less susceptible to collecting emissions from multiple surface types within one measurement.

As a final comparison, AMSR2 T_B values were compared to *in situ* sea ice thermophysical properties in order to derive a relationship between stage of melt and passive microwave signature. Stations experiencing a low SIC or high cloud cover within the extent of the AMSR2 footprint were excluded, leaving four stations for the final analysis. The remaining stations were divided into stages of melt, based on the ice surface thermophysical properties at each station: late spring (station 25), early melt (station 11) and advanced melt (stations 36 and 38). AMSR2 and *in situ* T_B increased for all frequencies/polarizations, particularly for 37 and 89 GHz, between late spring and early melt due to the introduction of liquid water in the snowpack during early melt. PR for all frequencies also decreased between late spring and early melt. GR(89/19H) decreased between early melt and advanced melt, with ratio values progressing from negative to positive. These results agree well with results from *in situ* T_B comparison with thermophysical sea ice surface properties.

5.1 Significance

Satellite-based sea ice concentration retrievals during the summer melt period are notably inaccurate due to the evolution of sea ice thermophysical properties throughout this period (Rösel et al. 2012b; Ivanova et al. 2015). The spring and summer months are of particular importance for maritime activities in Hudson Bay, due to the transition from a fully ice-covered to ice-free sea surface in 3 months (Gagnon and Gough, 2005). Breakup of the ice pack allows for the opening of commercial shipping routes and ceases local hunting operations in off-shore locations (Andrews et al., 2017). Predictions of the timing and rate of ice pack breakup within Hudson Bay can better inform future maritime operations, for which accurate sea ice concentration products are required.

To our knowledge, previous research on *in situ* T_B of sea ice throughout the summer melt period in Hudson Bay does not exist. This study contributes to this field by providing a comprehensive analysis of the co-evolution of *in situ* T_B and sea ice thermophysical properties throughout the melt period in Hudson Bay. Direct comparisons between *in situ* T_B and satellite-retrieved T_B throughout the sea ice melt period have not been reported, which limits our knowledge of the accuracy of SIC retrievals and detection of sea ice thermophysical properties. This study relates *in situ* T_B and AMSR2 T_B throughout the melt season, using SIC algorithm products and optical satellite imagery to facilitate the comparison. In this sense, it is the first study of its kind, and thus provides a basis for adopting data integration methods in future multi-scale passive microwave studies.

Data Accessibility Statement

Data collected during the 2018 BaySys expedition is publicly available on the Canadian Watershed Information Network (CanWIN; https://doi.org/10.5203/f35j-0t29).

Appendix

Table A1: Mean fractional reflectance values within each optical band for each sea ice surface class, used for UAV-supervised image classification during early melt. DOI: https://doi.org/10.1525/elementa.412.A1

Sea ice surface class	Mean fractional reflectance value[a]		
	Red (600 nm)	Green (540 nm)	Blue (460 nm)
Melt Pond	0.43	0.52	0.51
Open Water	0.03	0.04	0.04
Sea Ice	0.67	0.70	0.70

[a] Wavelengths for peak sensitivities of the DJI Phantom 4 sensor within each spectral colour band are provided in parentheses.

Table A2: Mean fractional reflectance values within each optical band for each sea ice surface class, used for UAV-supervised image classification during late melt. DOI: https://doi.org/10.1525/elementa.412.A2

Sea ice surface class	Mean fractional reflectance value[a]		
	Red (600 nm)	Green (540 nm)	Blue (460 nm)
Melt Pond	0.27	0.44	0.42
Open Water	0.05	0.06	0.06
Sea Ice	0.57	0.58	0.59

[a] Wavelengths for peak sensitivities of the DJI Phantom 4 sensor within each spectral colour band are provided in parentheses.

Acknowledgements

Data collection for this research would not be possible without the support and hospitality of the CCGS *Amundsen* crew during the 2018 field season, and the constant observations of sea ice conditions by the *Amundsen* wheelhouse throughout the duration of expedition. The authors would personally like to thank Laura Dalman and David Babb from the University of Manitoba for assistance during physical ice sampling, and Kevin Sydor and Karen Wong from Manitoba Hydro for their input during manuscript revision. This work benefitted from the contributions of two anonymous reviewers, associate editor Stephen Ackley, and editor-in-chief Jody Deming, whose extensive comments during the revision process greatly improved the final manuscript. Thank you to the Japan Aeronautics Exploration Agency (JAXA) for supplying AMSR2 data, and to the G-Portal Support Desk for timely responses regarding clarification for AMSR2 T_B data. This research contributes to the ArcticNet Networks of Centers of Excellence and the Arctic Science Partnership (ASP).

Funding Information

This work is a contribution to the Natural Sciences and Engineering Council of Canada (NSERC) Collaborative Research and Development (CRD) project titled Hudson Bay System Study (BaySys). Funding for this research was graciously provided by the University of Manitoba Graduate Fellowship (UMGF), NSERC Discovery Grant (DGB and DI), Northern Scientific Training Program (NSTP), Manitoba Hydro, Amundsen Science, and the Canada Research Chairs program.

Competing Interests

The authors have no competing interests to declare.

Author Contributions

- Contributions of conception, design, data analysis, and manuscript draft: MLH
- Contributions to data acquisition: MLH, WC
- Contributions to data interpretation: MH, DI, WC
- Article revision: MLH, WC, DI, DGB

References

Andrews, JS, Babb, D and **Barber, DG.** 2017. Climate change and sea ice: Shipping acessibility on the marine transportation corridor through Hudson Bay and Hudson Strait (1980–2014). *Elem Sci Anth* **5**(15). DOI: https://doi.org/10.1525/elementa.130

Asmus, KW and **Grant, C.** 1999. Surface based radiometer (SBR) data acquisition system. *Int J Remote Sens* **20**(15–16): 3125–3129. DOI: https://doi.org/10.1080/014311699211651

Bliss, AC, Steele, M, Peng, G and **Meier, WN.** 2019. Regional variability of Arctic sea ice seasonal change climate indicators from a passive microwave climate data record. *Environ Res Lett* **14**: 1–11. DOI: https://doi.org/10.1088/1748-9326/aafb84

Cavalieri, DJ, Burns, BA and **Onstott, RG.** 1990. Investigation of the effects of summer melt on the calculation of sea ice concentration using active and passive microwave data. *J Geophys Res* **95**(C4): 5359–5369. DOI: https://doi.org/10.1029/JC095iC04p05359

Cavalieri, DJ, Gloersen, P and **Campbell, WJ.** 1984. Determination of sea ice parameters with the Nimbus-7 SMMR. *J Geophys Res* **89**(ND4): 5355–5369. DOI: https://doi.org/10.1029/JD089iD04p05355

Comiso, JC. 2009. Enhanced sea ice concentrations and ice extents from AMSR-E data. *J Remote Sens Soc Japan* **29**(1): 199–215. DOI: https://doi.org/10.11440/rssj.29.199

Comiso, JC, Cavalieri, DJ, Parkinson, CL and **Gloersen, P.** 1997. Passive microwave algorithms for sea ice concentration: A comparison of two techniques. *Remote Sens Environ* **60**(96): 357–384. DOI: https://doi.org/10.1016/S0034-4257(96)00220-9

Comiso, JC, Grenfell, TC, Bell, DL, Lange, MA and **Ackley, SF.** 1989. Passive microwave in situ observations of winter Weddell Sea ice. *J Geophys Res* **94**(C8): 10891–10905. DOI: https://doi.org/10.1029/JC094iC08p10891

Dawson, J, Porta, L, Okuribido-Malcolm, S, DeHann, M and **Mussells, O.** 2016. Northern Marine Transportation Corridors Workshop. *Proceedings of the Northern Marine Transportation Corridors Workshop*. Vancouver, BC: uO Research: Ottawa, ON.

Derksen, C, Toose, P, Lemmetyinen, J, Pulliainen, J, Langlois, A, Rutter, N and **Fuller, MC.** 2012. Evaluation of passive microwave brightness temperature simulations and snow water equivalent retrievals through a winter season. *Remote Sens Environ* **117**(January 2011): 236–248. DOI: https://doi.org/10.1016/j.rse.2011.09.021

de Winter, JCF. 2013. Using the student's t-test with extremely small sample sizes. *Pract Assessment, Res Eval* **18**(10): 1–12.

Du, JY, Kimball, JS, Shi, J, Jones, LA, Wu, S, Sun, R and **Yang, H.** 2014. Inter-calibration of satellite passive microwave land observations from AMSR-E and AMSR2 using overlapping FY3B-MWRI sensor measurements. *Remote Sens* **6**(9): 8594–8616. DOI: https://doi.org/10.3390/rs6098594

Eppler, DT, Farmer, LD, Lohanick, AW, Anderson, MR, Cavalieri, DJ, Comiso, JC, Gloersen, P, Garrity, C, Grenfell, TC, Hallikainen, M, Maslanik, JA, Matzler, C, Melloh, RA, Rubinstein, I and **Swift, CT.** 1992. Passive microwave signatures of sea ice. In: Carsey, FD, editor. *Microwave Remote Sensing of Sea Ice*, 47–71. American Geophysical Union. DOI: https://doi.org/10.1029/GM068p0047

ESRI. 2016. ArcGIS Release 10.5. Redlands, CA.

Gagnon, AS and **Gough, WA.** 2005. Trends in the dates of ice freeze-up and breakup over Hudson Bay, Canada. *Arctic* **58**(4): 370–382. DOI: https://doi.org/10.1007/s10584-005-1815-8

Gough, WA, Cornwell, AR and **Tsuji, LJS.** 2004. Trends in seasonal sea ice duration in southwestern Hudson Bay. *Arctic* **57**(3): 299–305. DOI: https://doi.org/10.14430/arctic507

Grenfell, TC. 1986. Surface-based passive microwave observations of sea ice in the Bering and Greenland seas. *IEEE Trans Geosci Remote Sens* **GE-24**(3): 378–382. DOI: https://doi.org/10.1109/TGRS.1986.289595

Harasyn, ML, Isleifson, D and **Barber, DG.** 2019. The influence of surface sediment presence on observed passive microwave brightness temperatures of first year sea ice during the summer melt period. *Can J Remote Sens* **0**(0): 1–17. Taylor & Francis. DOI: https://doi.org/10.1080/07038992.2019.1625759

Hochheim, KP and **Barber, DG.** 2010. Atmospheric forcing of sea ice in Hudson Bay during the fall period, 1980–2005. *J Geophys Res* **115**(C5): 1–20. DOI: https://doi.org/10.1029/2009JC005334

Hochheim, KP and **Barber, DG.** 2014. An update on the ice climatology of the Hudson Bay system. *Arctic, Antarct Alp Res* **46**(1): 66–83. DOI: https://doi.org/10.1657/1938-4246-46.1.66

Hwang, BJ, Ehn, JK, Galley, R and **Barber, DG.** 2007. Passive microwave signatures of autumnal sea ice types from ship-based observation. *Int Geosci Remote Sens Symp*, 4245–4248. DOI: https://doi.org/10.1109/IGARSS.2007.4423788

Ivanova, N, Pedersen, LT, Tonboe, RT, Kern, S, Heygster, G, Lavergne, T, Sørensen, A, Saldo, R, Dybkjær, G, Brucker, L and **Shokr, M.** 2015. Intercomparison and evaluation of sea ice algorithms: Towards further identification of challenges and optimal approach using passive microwave observations. *Cryosphere* **9**(5): 1797–1817. DOI: https://doi.org/10.5194/tc-9-1797-2015

JAXA. 2013. Data Users' Manual for the Advanced Microwave Scanning Radiometer 2 (AMSR2) onboard the Global Change Observation Mission 1st -Water "SHIZUKU" (GCOM-W1).

Kaleschke, L, Heygster, G, Lüpkes, C, Bochert, A, Hartmann, J, Haarpaintner, J and **Vihma, T.** 2001. SSM/I sea ice remote sensing for mesoscale ocean-atmosphere interaction analysis. *Can J Remote Sens* **27**(5): 526–537. DOI: https://doi.org/10.1080/07038992.2001.10854892

Karvonen, J. 2014. A sea ice concentration estimation algorithm utilizing radiometer and SAR data. *Cryosphere* **8**(5): 1639–1650. DOI: https://doi.org/10.5194/tc-8-1639-2014

Kern, S, Rösel, A, Toudal Pedersen, L, Ivanova, N, Saldo, R and **Tage Tonboe, R.** 2016. The impact of melt ponds on summertime microwave brightness temperatures and sea-ice concentrations. *Cryosphere* **10**(5): 2217–2239. DOI: https://doi.org/10.5194/tc-10-2217-2016

Lavergne, T, Macdonald Sørensen, A, Kern, S, Tonboe, R, Notz, D, Aaboe, S, Bell, L, Dybkjær, G, Eastwood, S, Gabarro, C, Heygster, G, Killie, MA, Kreiner, MB, Lavelle, J, Saldo, R, Sandven, S and **Pedersen, LT.** 2019. Version 2 of the EUMETSAT OSI SAF and ESA CCI sea-ice concentration climate data records. *Cryosphere* **13**(1): 49–78. DOI: https://doi.org/10.5194/tc-13-49-2019

Markus, T and **Cavalieri, DJ.** 2000. An enhancement of the NASA team sea ice algorithm. *IEEE Trans Geosci Remote Sens* **38**(3): 1387–1398. DOI: https://doi.org/10.1109/36.843033

Markus, T, Cavalieri, DJ, Gasiewski, AJ, Klein, M, Maslanik, JA, Powell, DC, Boba, Stankov, B, Stroeve, JC and **Sturm, M.** 2006. Microwave signatures of snow on sea ice: Observations. *IEEE Trans Geosci Remote Sens* **44**(11): 3081–3089. DOI: https://doi.org/10.1109/TGRS.2006.883134

Matzler, C, Ramseier, RO and **Svendsen E.** 1984. Polarization Effects in Sea-Ice Signatures. *IEEE J Ocean Eng* **9**(5): 333–338. DOI: https://doi.org/10.1109/JOE.1984.1145646

Meier, WN, Markus, T and **Comiso, JC.** 2018. AMSR-E/AMSR2 Unified L3 Daily 12.5 km Brightness Temperatures, Sea Ice Concentration, Motion & Snow

Depth Polar Grids, Version 1. [Level 3 Sea Ice 12 km]. Boulder, Colorado, USA: NASA National Snow and Ice Data Center Distributed Active Archive Center. [22 July 2019]. DOI: https://doi.org/10.5067/RA1MIJOYPK3P

Meier, WN, Markus, T, Comiso, JC, Ivanoff, A and **Miller J.** 2017. AMSR2 Sea Ice Algorithm Theoretical Basis Document. Greenbelt, MD.

Onstott, RG, Grenfell, TC, Matzler, C, Luther, CA and **Svendsen, EA.** 1987. Evolution of microwave sea ice signatures during early summer and midsummer in the marginal ice zone. *J Geophys Res Ocean* **92**(C7): 6825–6835. DOI: https://doi.org/10.1029/JC092iC07p06825

Peng, G and **Meier, WN.** 2018. Temporal and regional variability of Arctic sea-ice coverage from satellite data. *Ann Glaciol* **59**(76pt2): 191–200. DOI: https://doi.org/10.1017/aog.2017.32

Perovich, DK. 2002. Aerial observations of the evolution of ice surface conditions during summer. *J Geophys Res* **107**(C10): 8048. DOI: https://doi.org/10.1029/2000JC000449

Radiometrics. 2004. AC1900 19 GHz, AC3700 37 GHz, AND AC8900 89 GHz dual polarization radiometers.

Rösel, A, Kaleschke, L and **Birnbaum, G.** 2012a. Melt ponds on Arctic sea ice determined from MODIS satellite data using an artificial neural network. *Cryosph* **6**(2): 431–446. DOI: https://doi.org/10.5194/tc-6-431-2012

Rösel, A, Kaleschke, L, Kern S, Rosel, A and **Kaleschke, L.** 2012b. Influence of melt ponds on microwave sensors' sea ice concentration retrieval algorithms. *Int Geosci Remote Sens Symp* (May 2014): 3261–3264. DOI: https://doi.org/10.1109/IGARSS.2012.6350608

Rostosky, P, Spreen, G, Farrell, SL, Frost, T, Heygster, G and **Melsheimer, C.** 2018. Snow depth retrieval on Arctic sea ice from passive microwave radiometers — improvements and extensions to multiyear ice using lower frequencies. *J Geophys Res Ocean* **123**: 7120–7138. DOI: https://doi.org/10.1029/2018JC014028

Spreen, G, Kaleschke, L and **Heygster, G.** 2008. Sea ice remote sensing using AMSR-E 89-GHz channels. *J Geophys Res Ocean* **113**(2): 1–14. DOI: https://doi.org/10.1029/2005JC003384

Toyota, T, Haas, C and **Tamura, T.** 2010. Size distribution and shape properties of relatively small sea-ice floes in the Antarctic marginal ice zone in late winter. *Deep Res Part II Top Stud Oceanogr* **58**(9–10): 1182–1193. Elsevier. DOI: https://doi.org/10.1016/j.dsr2.2010.10.034

Ulaby, FT and **Long, DG.** 2014. *Microwave Radar and Radiometric Remote Sensing*. London, UK: University of Michigan Press. DOI: https://doi.org/10.3998/0472119356

How to cite this article: Harasyn, ML, Isleifson, D, Chan, W and Barber, DG. 2020. Multi-scale observations of the co-evolution of sea ice thermophysical properties and microwave brightness temperatures during the summer melt period in Hudson Bay. *Elem Sci Anth,* 8: 16. DOI: https://doi.org/10.1525/elementa.412

Domain Editor-in-Chief: Jody W. Deming, School of Oceanography, University of Washington, US

Associate Editor: Stephen F. Ackley, Department of Geological Sciences, University of Texas at San Antonio, US

Knowledge Domain: Ocean Science

Part of an *Elementa* Special Feature: BaySys

Submitted: 24 August 2019 **Accepted:** 28 March 2020 **Published:** 23 April 2020